Draft version March 5, 2026
Typeset using LaTeX **twocolumn** style in AASTeX7

Bulge+Disk Morphology in Rest-frame UV and Optical: Size–Mass Relations Reveal Distinct Growth Paths for Star-forming and Quiescent Galaxies

Angelo George (喬安哲) [1,2] Ivana Damjanov [1,*] Marcin Sawicki [1] Stéphane Arnouts [3] Lingjian Chen [1] Guillaume Desprez [1] Stephen Gwyn [4] Thibaud Moutard [5] Michele Pizzardo [1,6] Anna Sajina [7] and Devin J. Williams [1]

[1] *Institute for Computational Astrophysics and Department of Astronomy & Physics, Saint Mary's University, 923 Robie Street, Halifax, Nova Scotia, B3H 3C3, Canada*
[2] *Institute for Astronomy and Astrophysics, Academia Sinica, No.1, Sec. 4, Roosevelt Rd, Taipei 106319, Taiwan*
[3] *Aix Marseille Université, CNRS, CNES, LAM, 38 rue Frédéric Joliot-Curie, Marseille 13388 cedex 13, France*
[4] *NRC Herzberg Astronomy and Astrophysics, 5071 West Saanich Road, Victoria, British Columbia, V9E 2E7, Canada*
[5] *European Space Agency (ESA), European Space Astronomy Centre (ESAC), Camino Bajo del Castillo s/n, 28692 Villanueva de la Cañada, Madrid, Spain*
[6] *Institute for Astronomy and Astrophysics, Academia Sinica, Taipei 106319, Taiwan*
[7] *Department of Physics and Astronomy, Tufts University, Medford, MA 02155, USA*

ABSTRACT

We characterize the structural evolution of a mass-complete sample of 44,000 star-forming galaxies (SFGs) and 34,000 quiescent galaxies (QGs) at $0.1 < z < 0.85$ using the CFHT CLAUDS and Subaru HSC-SSP datasets. By performing bulge+disk decompositions in both rest-frame UV (3000 Å) and optical (5000 Å), we provide the first statistical dual-wavelength analysis of the size–mass relation for these individual components. At a fiducial mass of $M_* = 5 \times 10^{10}\ M_\odot$, disk sizes are consistently larger than their corresponding bulges, with this disparity being more pronounced in the UV. We find that both components are larger in SFGs than in QGs. Notably, disks are more extended in the UV than in the optical, while bulge sizes remain comparable across both wavelengths. The pace of size evolution (measured as $R_e \propto (1+z)^\beta$) is wavelength-dependent: QG disks grow significantly faster in the optical ($\beta = -0.99$) than in the UV ($\beta = -0.49$), whereas bulges exhibit the opposite trend, with faster growth in the UV ($\beta = -1.51$) than in the optical ($\beta = -1.02$). SFG components show similar but less pronounced trends, with disks evolving at $\beta = -0.53$ (UV) and -0.64 (optical), whereas bulges evolve at $\beta = -1.09$ (UV) and -0.70 (optical). Our results suggest that bulge growth primarily drives the size evolution of SFGs, while the structural assembly of QGs is governed by a combination of steady influx of recently quenched 'newcomers' and minor mergers/accretion.

Keywords: Galaxies (573) — Galaxy evolution (594) — Ultraviolet astronomy (1736) — Optical astronomy (1776)

1. INTRODUCTION

Galaxies assemble their stellar mass through a combination of processes — including star formation, mergers, gas accretion, and feedback — that leave observable signatures in their stellar light distributions, such as sizes, surface brightness profiles, and morphologies, over cosmic time. Quantifying these structural properties and tracing their evolution therefore provides a direct observational route to constraining the physical mechanisms that govern galaxy formation and evolution (e.g., R. J. Buta 2013; C. J. Conselice 2014).

A long-established and widely adopted approach to characterizing galaxy structure is to decompose their light profiles into two primary components: a centrally concentrated bulge and an extended disk (P. D. Allen et al. 2006; L. Simard et al. 2011; C. N. Lackner & J. E. Gunn 2012; J. T. Mendel et al. 2014; M. Vika et al. 2014; R. Kennedy et al. 2016; R. Lange et al. 2016; P. Dimauro et al. 2018; C. Bottrell et al. 2019; B. Häußler et al. 2022; S. Casura et al. 2022; L. Quilley & V. de Lapparent 2022; L. Quilley & V. de Lapparent 2023; E. Merlin et al. 2023; Euclid Collaboration et al. 2023; K. Jegatheesan et al.

Email: angelogeorget@gmail.com
* Canada Research Chair

2024; L. Quilley et al. 2025; L. Kawinwanichakij et al. 2025, among many others). Empirically, disks are typically larger in size and well described by exponential light profiles, while bulges are more compact and centrally concentrated (K. C. Freeman 1970; J. Kormendy 1977; C. M. Carollo et al. 1997; P. Lang et al. 2014; J. Méndez-Abreu et al. 2021; A. S. G. Robotham et al. 2022a; C. Lima-Dias et al. 2024; L. Kawinwanichakij et al. 2025). Beyond their distinct spatial distributions, bulges and disks also differ systematically in their stellar population properties — such as ages, star formation activity, and chemical enrichment — indicating that they trace different modes of mass assembly and evolutionary pathways (e.g., J. Kormendy & R. C. Kennicutt 2004; S. Khochfar & J. Silk 2006; D. B. Fisher & N. Drory 2011; C. Tonini et al. 2016; B. Clauwens et al. 2018; L. Zhang et al. 2025).

An important and widely used scaling relation for linking galaxy structure to stellar mass assembly is the size–mass relation (SMR). Because it connects mass growth to structural growth, the SMR provides a sensitive probe of the physical processes — such as mergers, tidal interactions, emergence of bulges, fading of disks, etc. — that shape galaxies over cosmic time. It is now well established that the total sizes of galaxies scale with their stellar mass, and that star-forming galaxies (SFGs) and quiescent galaxies (QGs) have their own sequences in the size–mass plane (e.g., S. Shen et al. 2003; I. Trujillo et al. 2004; Y. Guo et al. 2009; R. J. Williams et al. 2010; A. B. Newman et al. 2012; A. van der Wel et al. 2014; R. Lange et al. 2015; A. L. Faisst et al. 2017; N. Roy et al. 2018; L. A. Mowla et al. 2019; J. Matharu et al. 2019, 2020, 2024; I. Damjanov et al. 2019, 2023; L. Kawinwanichakij et al. 2021, 2025; S. E. Cutler et al. 2022; A. George et al. 2024, 2025; K. Ito et al. 2024; M. Martorano et al. 2024; E. Ward et al. 2024; K. Ormerod et al. 2024).

With the advent of deep, high-resolution imaging, it has become possible to extend this analysis to individual structural components. Recent studies have demonstrated that both bulges and disks follow their own SMRs, which share a similar linear functional form in logarithmic space but differ in slope and normalization (V. A. Bruce et al. 2014; P. Dimauro et al. 2019; A. Hashemizadeh 2022; D. S. H. Hon et al. 2023; K. V. Nedkova et al. 2024; R. H. W. Cook et al. 2025; L. Kawinwanichakij et al. 2025, among others). This implies that the observed SMRs of whole SFGs and QGs largely reflect the combined contributions of their bulge and disk components. Component-resolved SMRs therefore offer a powerful framework for testing theoretical models of galaxy formation, as they place direct constraints on how stellar mass is assembled spatially within galaxies and how different physical processes shape bulges and disks across cosmic time.

Despite significant progress, existing studies of bulge and disk SMRs remain limited by sample size, survey area, and redshift coverage. Many of the component-resolved analyses are based on a few hundred to a few thousand galaxies, typically drawn from deep but narrow fields ($\lesssim 2$ deg^2), which makes them susceptible to cosmic variance and limits statistical power (e.g., V. A. Bruce et al. 2014; P. Dimauro et al. 2019; J. Méndez-Abreu et al. 2021; A. Hashemizadeh 2022; D. S. H. Hon et al. 2023; K. V. Nedkova et al. 2024). In addition, many studies probe only a small restricted redshift interval or focus on single epochs, limiting their ability to robustly trace the evolution of bulges and disks (e.g., J. Méndez-Abreu et al. 2021; A. S. G. Robotham et al. 2022a; D. S. H. Hon et al. 2023). These limitations motivate the need for wide-area surveys that enable component-resolved structural measurements for large, representative samples out to intermediate redshifts.

So far, works in the literature have primarily looked at the SMR of bulges and disks only in a single rest-frame wavelength. The preferred choice so far has been in the optical/near-IR regime, as the light in these wavelengths traces the distribution of old and low-mass stars that form the bulk of the stellar population in galaxies (G. Bruzual & S. Charlot 2003; D. C. Martin et al. 2005). However, in our pilot study (A. George et al. 2024, hereafter Paper I), we showed that it is also vital to analyze galaxy morphologies in rest-frame UV to study the distribution of young and/or low-metallicity stars. By contrasting the structural properties of the rest-UV and rest-optical, we could identify the physical processes driving the galaxy evolution. For example, the growth driven by minor mergers should increase the average of sizes of galaxies with similar mass faster in rest-UV than in the rest-optical as shown by our earlier works, Paper I and A. George et al. (2025, hereafter Paper II). Similarly, inside-out quenching — due to AGN feedback, growth of bulges, etc. — should make the galaxy sizes smaller in the longer wavelength.

Therefore, in this work, for the first time, we analyze the morphologies and the redshift evolution of the SMR for bulges and disks of SFGs and QGs in two rest-frame wavelengths (UV and optical) over 6 billion years ($0.1 < z < 0.85$). We utilize the deep multi-wavelength dataset from the CFHT CLAUDS (M. Sawicki et al. 2019) and Subaru HSC-SSP (H. Aihara et al. 2018, 2019) surveys that cover a sky area of 18.6 deg^2.

Quantifying the structural evolution of bulges and discs requires a choice of mass-anchor, with existing

studies generally adopting one of two complementary strategies. Some studies compute component SMRs using bulge and disk stellar masses (e.g., V. A. Bruce et al. 2014; P. Dimauro et al. 2019; A. Hashemizadeh 2022; A. S. G. Robotham et al. 2022a; K. V. Nedkova et al. 2024; R. H. W. Cook et al. 2025), while others relate component sizes to the total stellar mass of the host galaxy (e.g., C. Tonini et al. 2016; J. Méndez-Abreu et al. 2021; L. Kawinwanichakij et al. 2025). These complementary approaches respectively probe the intrinsic evolution of individual components and their growth in the context of the galaxy as a whole.

To consistently compare structural components across this large and diverse sample, we adopt the total stellar mass of the galaxy, rather than the component mass, when analyzing the SMRs of bulges and disks. Since stellar mass is a fundamental property closely linked to various galaxy characteristics (E. F. Bell et al. 2003; B. Panter et al. 2004; I. K. Baldry et al. 2006; Y.-j. Peng et al. 2010; S. Zibetti & A. R. Gallazzi 2022), this approach allows us to compare the characteristic sizes of bulges and disks in galaxies of similar stellar mass, and, thus, similar global properties.

This paper is divided into the following sections. We provide an overview of the dataset used in Section 2. Section 3 describes the methodology we adopt to measure the morphological properties (especially the size) of the structural components of the SFGs and QGs through decomposition into a bulge and disk in two rest-frame wavelengths. We then analyze the size-stellar mass relation for bulges and disks in Section 5 and the evolution of the characteristic sizes (SMR zero points) for these structural components in Section 6. Section 7 provides the interpretation of the results for SFGs (Section 7.1) and QGs (Section 7.2). We address potential caveats and methodological limitations in Section 8. Finally, we summarize our major findings in Section 9.

Throughout this work, we use M to denote stellar mass in solar units ($M_\star/\mathrm{M}_\odot$) unless otherwise stated. Additionally, we use the AB magnitude system and adopt a standard cosmology with $\Omega_M = 0.3$, $\Omega_\Lambda = 0.7$ and $H_0 = 70$ km/s/Mpc throughout this paper.

2. DATA

2.1. *Dataset Overview and Galaxy Classification*

For this work, we utilize the same data images and ancillary data as in Paper II. In short, we use the Deep and UltraDeep multi-band ($U+griz$) imaging data from the CFHT Large Area U-band Deep Survey[8] (CLAUDS; M. Sawicki et al. 2019) and the Hyper Suprime-Cam Subaru Strategic Program[9] (HSC-SSP; H. Aihara et al. 2018, 2022) covering 18.6 deg^2 spanning over four survey fields (E-COSMOS, DEEP2-3, ELAIS N1 and XMM-LSS). We also have complementary imaging from the SHIRAZ Survey (M. Annunziatella et al. 2023, IRAC 3.6m and 4.5m) in the E-COSMOS, DEEP2-3 and ELAIS N1 fields, and the VIRCAM near-IR wavelength coverage (Y, J, H, and K_s bands) from the VIDEO (M. J. Jarvis et al. 2013) and UltraVISTA (H. J. McCracken et al. 2012) surveys over a combined 5.5 deg^2 across the E-COSMOS and XMM-LSS fields.

Similar to Paper II, we rely on the CLAUDS+HSC photometric catalog by G. Desprez et al. (2023) made with the HSC Pipeline (hscPipe; J. Bosch et al. 2018) to select our galaxy sample. Photometric redshift estimates are based on *Ugrizy* or *Ugrizy*+*JHK*$_s$ (where VISTA *JHK*$_s$ bands are available) and calculated using Phosphoros[10] (Euclid Collaboration et al. 2020; Paltani et al. in preparation), a template fitting code created to be part of the Euclid photo-z pipeline. These photo-z measurements have a precision of 0.05 and a very small fraction of outliers ($< 6\%$ at $i < 25$; G. Desprez et al. 2023).

Estimation of other galaxy properties that we use (stellar masses and rest-frame colors) are based on *Ugrizy* photometry together with VISTA *JHK*$_s$ (in the XMM-LSS field) or IRAC Ch1 and Ch2 (in the other three fields) using LePhare (O. Ilbert et al. 2006) template-fitting code. This is done by fixing the redshifts of galaxies to the photometric redshift values from G. Desprez et al. (2023) and assuming the Chabrier initial mass function (IMF; G. Chabrier 2003) and an exponentially decaying star formation history. Following the approach of T. Moutard et al. (2016), dust extinction is modeled using a range of attenuation laws: M. L. Prevot et al. (1984), D. Calzetti et al. (2000), and a modified Calzetti curve that incorporates a bump at 2,175Å. We will present the detailed procedure for these estimations in L. Chen et al. (in preparation).

As in Paper II, we adopt a modified variant of the *NUVrK* color-color selection (S. Arnouts et al. 2013; T. Moutard et al. 2018, 2020) to classify our galaxies into star-forming and quiescent (L. Chen et al., in preparation). In short, to smoothly account for redshift and mass dependence, we adopt an *NUVrK* selection method based on the distribution of galaxies in a four-dimensional parameter space defined by *NUV*-*r*, *r*-*K*,

[8] https://www.clauds.net/

[9] https://hsc.mtk.nao.ac.jp/ssp/

[10] https://anaconda.org/astrorama/phosphoros

redshift and stellar mass. Our selection criteria for QGs are

$$\begin{aligned} NUV - r &> (c_1 z + c_2 \log M + c_3)[(r - K) + c_4], \\ NUV - r &> c_5, \end{aligned} \quad (1)$$

where the empirically calibrated values for constants $c_1 - c_5$ are 3.868, 2.397, 1.003, -0.278 and 0.039, respectively. Full details of the SFG/QG classification method for the CLAUDS+HSC sample will be available in L. Chen et al. (in preparation).

2.2. *Sample Mass Completeness*

We estimate the stellar mass completeness using the method of L. Pozzetti et al. (2010), which infers the limiting stellar mass by rescaling the stellar masses of individual galaxies to the survey flux limit and defining the mass above which a fixed fraction (85%) of galaxies would be observable. The resulting completeness limits are shown in Figure 1, with SFGs on the left and QGs on the right. The parent catalog is flux-limited to $i < 26$ to ensure reliable photo-z and contains stellar mass estimates for these galaxies. Based on this limit, the catalog is mass-complete down to $\log M \gtrsim 8.5$ for SFGs and $\log M \gtrsim 9$ for QGs at $z \leq 0.85$. These completeness limits are indicated by the yellow curves in the figure.

However, bulge-disk decomposition is not feasible for all galaxies in the parent catalog. As we show using simulations — similar to those in our previous works (Papers I & II) and discussed in Appendix A — we can reliably model structural components for bright galaxies with $i < 22$ mag. We thus restrict our structural analysis to this brighter subset. This i-band cut increases the stellar mass completeness thresholds to $\log M \gtrsim 10.8$ for SFGs and $\log M \gtrsim 11.0$ for QGs at $z > 0.7$. The completeness limits of the final SFG and QG samples we use throughout this study are represented by green curves in Figure 1.

Adopting a single mass limit across the full redshift range would require using the highest completeness threshold, corresponding to $\log M \gtrsim 10.8$ for SFGs and $\log M \gtrsim 11.0$ for QGs, which would severely reduce the available sample size. To retain a statistically large sample while maintaining mass completeness, we therefore adopt redshift-dependent stellar mass limits, defined within discrete redshift bins motivated by the SMR analysis in this work and in Paper II.

The black boxed regions in Figure 1 represent the selected sample with these evolving stellar mass limits. For SFGs, the adopted mass limits are: $\log M > 9.7$ ($0.1 < z < 0.4$), > 10.2 ($0.4 < z < 0.55$), > 10.5 ($0.55 < z < 0.7$), and > 10.8 ($0.7 < z < 0.85$). For QGs, the corresponding limits are: $\log M > 10.4$ ($0.1 < z < 0.55$), > 10.7 ($0.55 < z < 0.7$), and > 11.0 ($0.7 < z < 0.85$). We limit our QG sample with stellar mass $\log M > 10.4$ as we intend to analyze the QG SMR above its pivot point ($\log M \sim 10.4$; Papers I & II). We thus obtain a mass-complete sample of 44,086 SFGs and 34,108 QGs, as summarized in Table 1.

Category	**Number**
All objects ($i < 26$)	7,493,735
Galaxies with reliable mass measurements	5,239,677
$i < 23$	873,867
SE++ fits	569,464
UV	547,906
Optical	531,883
$i < 22$	262,168
$0.1 < z < 0.85$	221,575
$\log M > 9.7$	139,809
SFGs	84,420
QGs	55,389
Mass-complete sample:	
SFGs	44,086
QGs	34,108
Reliable SE++ fits in UV:	
SFGs	42,245
SFG Bulges†	16,654
SFG Disks‡	41,795
QGs	33,319
QG Bulges†	25,664
QG Disks‡	32,597
Reliable SE++ fits in Optical:	
SFGs	42,341
SFG Bulges†	21,376
SFG Disks‡	41,374
QGs	33,470
QG Bulges†	30,415
QG Disks‡	28,899
Reliable SE++ fits in UV & Optical:	
SFGs	41,210
QGs	32,885

Table 1. Sample selection from the CLAUDS+HSC data.
†Number of bulges with $B/T > 0.2$, used for SMR fits.
‡Number of disks with $B/T < 0.8$, used for SMR fits.

3. METHODOLOGY

To investigate the evolution of galaxy structural components separately, we perform two-component bulge+disk decompositions using SourceXtractor++[11] (SE++; E. Bertin et al. 2020), a modern

[11] https://ascl.net/2212.018

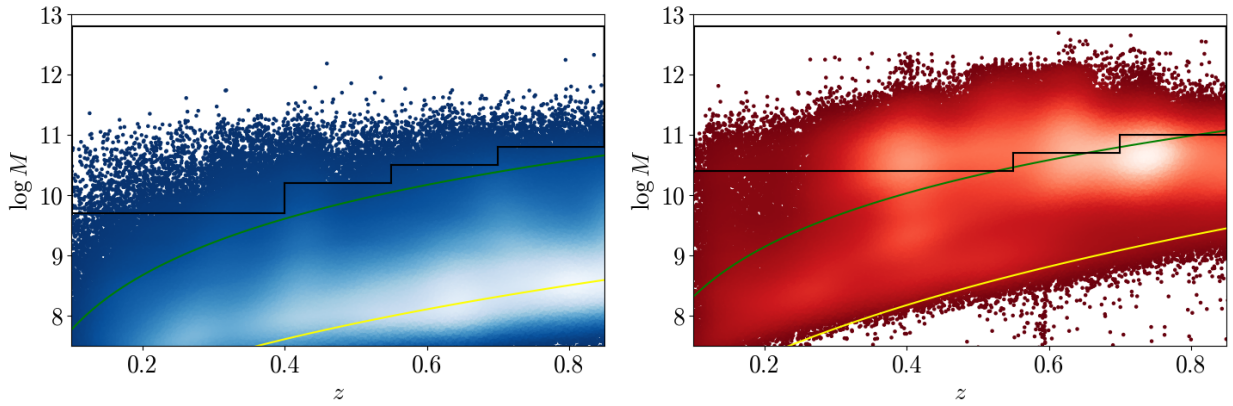

Figure 1. Left: Selection of mass complete sample for SFGs based on the magnitude cut ($i < 22$ mag) adopted in this work. The distribution of the SFGs from the parent catalog in the stellar mass-redshift space is shown in blue heatmap, and the yellow curve shows the 85% mass completeness limit for these SFGs. The 85% mass completeness limit after applying the magnitude cut is shown in green. The selected mass complete sample is shown within a black boxed region. Right: Selection of mass complete sample for similarly bright QGs, with mass completeness limit for QGs shown in green. The distribution of the QGs from the parent catalog is shown in red heatmap. Similar to the left panel, the selected QG sample is shown within the boxed region.

extension of SOURCE EXTRACTOR[12] (SEXTRACTOR; E. Bertin & S. Arnouts 1996; E. Bertin 2011), that enables simultaneous multi-component, multi-band structural fitting. Unlike SExtractor, which is primarily designed for source detection and basic photometry, SE++ allows parametric modeling of galaxy light profiles across multiple wavelengths in a unified framework. Using SE++, we model each galaxy with a Sérsic profile for the bulge component, where the Sérsic index n is left free, and an exponential profile for the disk component, corresponding to a fixed Sérsic index $n = 1$. This bulge+disk fits are performed across the *Ugriz* bands of the CLAUDS+HSC imaging separately. This multi-component fitting approach is analogous to our previous single-Sérsic analyses (Papers I & II), but enables us to isolate the sizes of bulges and disks individually and assess their distinct contributions to the observed structural evolution of galaxies.

Prior to structural fitting, SE++ identifies and segments galaxies using a model-based detection and deblending scheme. The software models light distributions by comparing observed pixel values to a parametric model convolved with local PSFs, which we generate for each field using the Point Spread Function Extractor[13] (PSFEX; E. Bertin 2011, 2013) and SEXTRACTOR. The fitting process minimizes a modified least-squares cost function weighted by pixel-level uncertainties. To ensure robustness against neighboring contamination or noise spikes, we set the modified χ^2 scale to 4; this processes residuals through a monotonic transformation that downweights large deviations to prevent outliers from biasing the fit. Furthermore, we utilize the iterative model-fitting mode with a maximum of 250 iterations and 5 meta-iterations to ensure stable convergence in these complex bulge-disk decompositions.

The SE++ configuration is optimized for robust fitting of galaxies with diverse morphologies. In general, we adopt the SE++ configurations and methodologies followed by the Euclid Collaboration recently (Euclid Collaboration et al. 2023; L. Quilley et al. 2025). We adopt a detection threshold of 5σ above the local background, estimated on a grid with `background-cell-size = 256` pixels to balance accuracy in crowded fields. The fitting model combines a Sérsic bulge (`x, y, flux`$_B$`, R`$_{e,B}$`, n`$_B$`, pa, q`$_B$) and an exponential disk (`x, y, flux`$_D$`, R`$_{e,D}$`, pa, q`$_D$), where `R`$_e$ is the effective radius along the semi-major axis, `n` is Sérsic index, `pa` is the position angle and `q` is the axis ratio. We use initial parameters derived from built-in functions for isophotal centroid, flux, size and position angle.

Beyond its robust cost function, SE++ offers advanced regularization capabilities that stabilize multi-component fits — a significant improvement over the original SEXTRACTOR. We leverage these features by defining physically motivated parameter ranges and informative Gaussian priors on the model parameters. For the bulge component, we implement a non-Gaussian prior on the Sérsic index, $N = \exp(n - n_0)$ with $n_0 = 6$. This serves to penalize unphysically high concentrations ($n > 7$) while remaining uninformative for lower indices ($n \lesssim 5$), a more conservative threshold than the $n_0 = 8$

[12] https://ascl.net/1010.064
[13] http://ascl.net/1301.001

adopted in a recent single Sérsic SE++ analysis by M. Pizzardo et al. (2026). To maintain a structural hierarchy, we also apply a joint prior on the relative sizes of the components: $\Delta \log R_e = \log_{10}(R_{e,B}) - (2\log_{10}(R_{e,D}) - 0.48)$. This regularization prevents non-physical solutions, such as component swapping, while allowing the final sizes to remain data-driven. We further stabilize the fit using a logit-normal prior on the bulge-to-total (B/T) ratio centered at $B/T \approx 0.1$ and constrain all axis ratios and radii using exponential ranges to avoid degenerate solutions.

Similar to Papers I & II, we test the robustness of the fitting methodology and estimate the uncertainties in the fit parameters obtained from SE++ through extensive simulations. We are able to model more than 90% of the simulated galaxies, and we use the spread in the measured parameters of these galaxies to estimate the uncertainties. Additionally, we also use the simulations to correct the biases present in our size measurements. Throughout this work, we adopt these corrected size estimates for analysis. We discuss these simulations, their results, uncertainty estimation and bias correction in Appendix A.

4. BULGES AND DISKS IN TWO REST-FRAME WAVELENGTHS

Following the methodology prescribed in Papers I & II, we estimate the structural parameters of bulge and disk components in two rest-frame wavelengths: 3000Å (UV) and 5000Å (optical). In short, we take a weighted average of structural parameters of a galaxy in the two nearest observed bands that either bracket or are close to the rest-frame 3000Å and 5000Å. In case of fit results available in only a single band that is close to the rest-frame wavelength, we simply adopt the results in that band. Thus, the observed bands we use to estimate the Sérsic parameters of bulges and disks in the same rest-frame regimes depend on the redshift of individual galaxies.

We have modeled the light profiles of 569,464 galaxies with $i < 23$ mag in the CLAUDS+HSC images, although after the cuts based on magnitude ($i < 22$ mag), redshift ($0.1 < z < 0.85$) and stellar mass for completeness, the final sample with bulge+disk decomposition used for analysis in this work contains 44,086 SFGs and 34,108 QGs. However, we note that not all galaxies have light profiles modeled in both rest-frame wavelengths. Thus, we have structural parameters for 42,245 SFGs in rest-UV and 42,341 SFGs in rest-optical. Similarly, the corresponding numbers for QGs are 33,319 and 33,470, respectively. Out of these, 41,210 SFGs and 32,885 QGs have structural component fits in both rest-frame wavelengths. We provide these numbers in Table 1. Because SE++ failed to model $\sim 5\%$ of the sample, excluding these "failed" galaxies won't affect our analysis.

The bulge and disk sizes used in this analysis have been calibrated against systematic offsets identified in our image simulations (Appendix A). For example, the pipeline, in general, overestimates the bulge sizes. Although this bias reaches $\sim 50\%$ if the measured $n_B > 4.5$, it is significantly lower ($\sim 10\%$) for bulges with $n_B < 4.5$ where majority of the observed galaxies are (Figure 11). In contrast, the biases in the measured disk sizes are significantly smaller than those of bulge sizes except for bulge dominated galaxies ($B/T > 0.75$) that do not constitute a dominant population in our disk analysis sample (Figure 12). Accordingly, we apply a correction to our bulge and disk size measurements to account for these systematic biases, as detailed in Appendix A.2. While all results presented hereafter utilize these bias-corrected measurements, we note that the qualitative trends of this work remain consistent even without these adjustments.

In addition, our simulations (Appendix A) indicate that although SE++ effectively models the overall galaxy light profile, the size measurements of individual structural components (i.e., bulge and disk) are reliable only when the component contributes at least 20% of the total modeled flux. In other words, we can robustly recover the size of a disk only if it is not overwhelmed by the bulge (and vice versa). Thus, in this work, we introduce cuts in the bulge-to-total (B/T) ratios while selecting galaxy bulges and disks for analysis. For bulge and disk components, these selection criteria are $B/T > 0.2$ and $B/T < 0.8$, respectively. The number of bulges and disks that meet these criteria is listed in Table 1. Similar B/T cuts have been adopted in previous studies (e.g., P. D. Allen et al. 2006; A. Meert et al. 2015; P. Dimauro et al. 2018, 2022; B. Häußler et al. 2022; Euclid Collaboration et al. 2023; A. Ghosh et al. 2023). Because the excluded bulges and disks have mass and redshift distributions similar to those of the parent bulge and disk populations, these B/T thresholds are not expected to introduce significant biases. Ultimately, our analysis focuses on the size evolution of bulges and disks in galaxies for which these components are sufficiently prominent to be reliably measured.

Figure 2 presents the distribution of effective radii for these *significant* bulge and disk components of SFGs (the top panels) and QGs (the bottom panels), measured in two rest-frame wavelengths. In this figure and throughout this work, we use cyan (UV) and blue (optical) colors for SFG disks and pink (UV) and red (optical) colors for QG disks. Likewise, we use green (UV) and

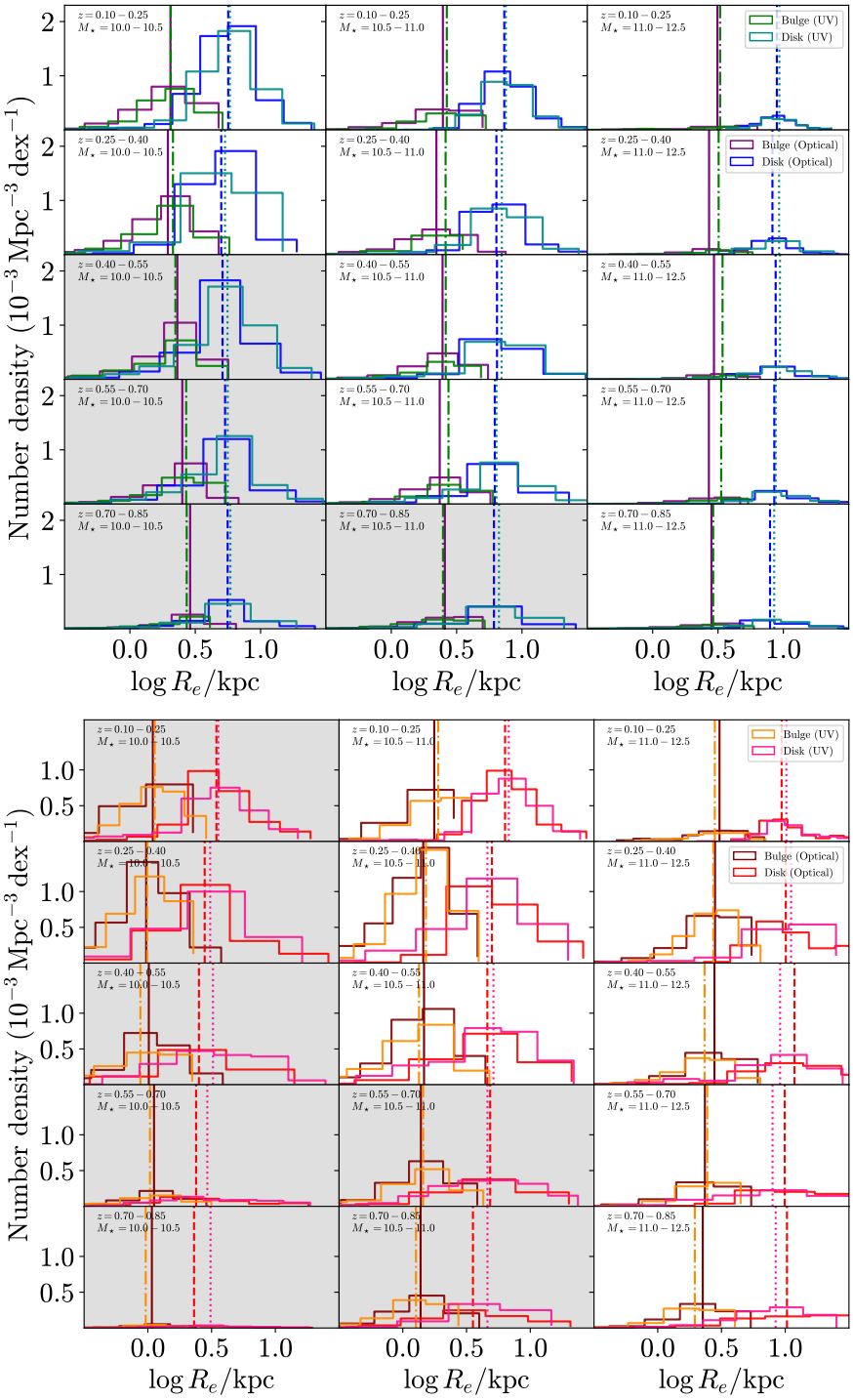

Figure 2. Top panels: Distribution of the sizes of the structural components of SFGs in rest-frame UV and optical wavelengths. The blue (purple) color denotes bulges in UV (optical), whereas the cyan (green) shows the distribution for disks in UV (optical). As we move from left to right, the stellar masses of the galaxies increase. Similarly, we move from lower to higher redshift bins downward. The y-axis shows the number density in comoving volume. The median values of $\log(R_e/\mathrm{kpc})$ for bulges and disks in UV and optical wavelengths in every panel are denoted by the vertical lines. We show the sizes of bulges only if the bulge-to-total ratio, $B/T > 0.2$, and we show the sizes of disks only if $B/T < 0.8$. The panels affected by sample mass incompleteness are shaded grey. Bottom panels: Distribution of the sizes of the structural components of QGs. The red (maroon) color represent bulges in UV (optical), while the pink (orange) represents disks in UV (optical).

purple (optical) colors for SFG bulges, and orange (UV) and maroon (optical) colors for QG bulges.

As expected, disks are generally more extended than bulges across both galaxy types and wavelengths, as indicated by the differences in their median sizes (vertical lines in Figure 2). This trend holds across all stellar mass ($\log M_\star > 10$) and redshift ($0.1 < z < 0.85$) bins. Disk size distributions are also significantly broader than those of bulges. In many bins, a non-negligible fraction of disks have effective radii smaller than the median bulge size, whereas bulges with sizes exceeding the median disk size in the same bin are extremely rare.

The sizes of bulges and disks depend on the stellar mass and redshift of galaxies. As expected, more massive galaxies tend to have larger bulges and disks irrespective of the wavelength or redshift bin. For example, in the rest-optical, SFG bulges (disks) at $0.4 < z < 0.55$ are 28% (71%) larger in the highest mass bin than in the lowest mass bin (third row in the top panels in Figure 2). For QGs, the differences are 174% and 370% for bulges and disks, respectively. The sizes of bulges and disks of both SFGs and QGs in the mass complete bins show a general negative trend with redshift in both wavelengths. As an example, the bulges and disks of the most massive ($\log M > 11$) SFGs grew by 12% and 13%, respectively, between the highest and lowest redshift bins in rest-optical (second column in the top panels in Figure 2). These trends with stellar mass and redshift reflect the similar trends we observe for global sizes of galaxies in our Paper I.

The sizes of galaxy components also depend on the rest-frame wavelength. Based on the median values in Figure 2, the disks are generally more extended in the rest-UV than in the optical wavelength, except for most massive QGs at $z > 0.4$. Bulges of SFGs tend be larger in the shorter wavelengths in the mass-complete bins. In contrast, QGs tend to have larger bulges in the longer wavelength in many of the bins.

We caution, however, that the plotted distributions do not account for uncertainties in the size measurements. While they effectively highlight overall trends, a more rigorous interpretation requires incorporating both measurement uncertainties and systematic effects. We address this by using size estimates derived from the SMR, which accounts for uncertainties in both mass and size measurements when estimating the characteristic sizes of galaxy components at a given stellar mass (Section 5).

The distribution of Sérsic indices of bulges (n_B) differs between SFGs and QGs (the top panel of Figure 3). In general, SFG bulges exhibit lower Sérsic indices than QG bulges, with typical values of $n_B < 2$ for SFGs and $n_B > 2$ for QGs. The SFG bulges tend to have more disk-like,

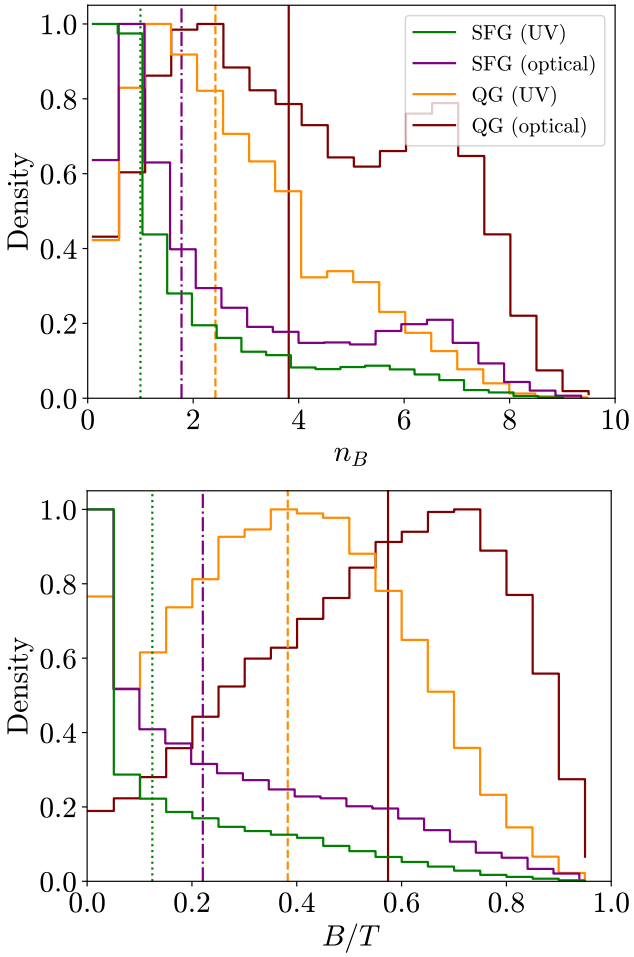

Figure 3. The top panel: Distribution of Sérsic indices of bulges in $\log M > 10.5$ galaxies with significant bulge component ($B/T > 0.2$). The green (purple) represent the SFG bulges in UV (optical) while the orange (maroon) represent the QG bulges in UV (optical). In each histogram, the bins are normalized to the value of the most populated bin. The vertical lines represent the median values. The bottom panel: Distribution of bulge-to-total (B/T) ratios for SFGs and QGs with stellar masses $\log M > 10.5$ in two rest-frame wavelengths. Rest of the details are same as in the top panel.

less centrally concentrated light profiles, while the QG bulges are generally more centrally concentrated.

The bulge Sérsic index also varies with rest-frame wavelength. Both SFGs and QGs show an increase in n_B at longer wavelengths, indicating that light profiles of the bulge components are more centrally concentrated in the rest-optical than in the rest-UV. Specifically, the median Sérsic index for $\log M > 10.5$ SFG bulges increases from 1.0 in the rest-UV to 1.8 in the rest-optical, while for $\log M > 10.5$ QG bulges it increases from 2.4 to 3.8. This trend is consistent with our previous single Sérsic analysis (Paper I). Since those single Sérsic profiles are strongly weighted by the highest surface brightness pix-

els near galaxy centers, their n-trend should follow the trend in n_B for non-negligible bulge components. This wavelength dependence of the central concentration of bulge profiles indicates that the older stellar populations, traced by rest-optical light, are more centrally concentrated in bulges than the younger stars, which dominate the rest-UV emission.

Despite the generally lower concentration of UV light, both SFGs and QGs display a high-n_B tail in the rest-UV distribution. Conversely, some optical bulges have $n_B \sim 1$. This suggests diversity in bulge properties, indicating that not all bulges are structurally similar. However, we caution that Sérsic index measurements derived from ground-based imaging are generally less robust than R_e estimates, particularly due to PSF effects (R. Davari et al. 2014; C. Dewsnap et al. 2023; A. George et al. 2024).

We also observe a secondary peak in the n_B distribution between $6 < n_B < 8$, particularly in the rest-optical. This feature likely reflects the influence of the non-Gaussian prior ($n_0 = 6$) applied during the structural fitting to prevent unphysically high concentrations (Section 3). In cases where the pixel data favors an extremely concentrated profile ($n \gtrsim 8$), the optimizer may settle within this penalized range. While this indicates that the highest n_B values should be interpreted as conservative lower limits, it does not affect our primary finding that QG bulges are significantly more concentrated than those of SFGs across both wavelengths.

The distribution of B/T ratios (the bottom panel of Figure 3) shows trends similar to those seen in the distributions of Sérsic indices of bulges . As expected, QGs exhibit higher B/T values than SFGs, indicating a more prominent bulge component in their light profiles. For example, 47% of SFGs with $\log M > 10.5$ have bulges contributing less than 20% of the total rest-optical light, compared to fewer than 10% among QGs.

Additionally, both SFGs and QGs tend to have higher B/T values in the rest-optical compared to the rest-UV, confirming that a higher fraction of older stellar population is located in bulges than in disks compared to the younger stellar population. For SFGs with stellar mass $\log M > 10.5$, the median B/T increases from 0.12 in the rest-UV to 0.22 in the rest-optical. In similarly massive QGs, the median values are 0.38 and 0.57, respectively. In terms of bulge dominance, 61% of QGs are bulge-dominated ($B/T > 0.5$) in the rest-optical, compared to 29% in the rest-UV. For SFGs, the corresponding fractions are significantly lower — 20% in the rest-optical and 11% in the rest-UV. However, as with Sérsic index measurements, we caution that B/T estimates are generally less robust than measurements of R_e of individual components that contribute significantly to the total light profile.

5. SIZE–MASS RELATIONS OF BULGES AND DISKS

With the bulge and disk sizes measured in two rest-frame wavelengths, we now examine the size–mass relation (SMR) of these structural components separately. The SMR is well established for star-forming and quiescent galaxies (e.g., S. Shen et al. 2003; R. J. Williams et al. 2010; A. van der Wel et al. 2014; L. A. Mowla et al. 2019; L. Kawinwanichakij et al. 2021, 2025; A. George et al. 2024, 2025), and has also been reported for bulges and disks in previous studies (e.g., V. A. Bruce et al. 2014; Y. Sofue 2016; P. Dimauro et al. 2019; A. Hashemizadeh 2022; D. S. H. Hon et al. 2023; K. V. Nedkova et al. 2024; R. H. W. Cook et al. 2025; L. Kawinwanichakij et al. 2025). Here, leveraging a statistically large and homogeneous sample over $0.1 < z < 0.85$, we extend these studies by providing a unified, multi-wavelength analysis of bulge and disk SMRs, which has so far been limited by sample size, redshift range, or the lack of consistent rest-frame wavelength comparisons.

We describe the SMR generally as

$$\log R_e = \log R_0 + \alpha \log\left(\frac{M}{M_0}\right) + \sigma_{\log R_e}, \qquad (2)$$

where α is the slope, R_0 is the characteristic size at a fiducial stellar mass M_0 and $\sigma_{\log R_e}$ is the intrinsic scatter in the linear regression. In this work, we use the effective radius (R_e) of the bulge and disk components and the total stellar mass (M) of the galaxy to construct the SMR. Similarly to our previous works, we adopt $M_0 = 5 \times 10^{10}$ $M_\odot$. While the slope of the SMR for QGs exhibits a transition at a pivot mass of $\log M = 10 - 10.4$ (e.g., A. van der Wel et al. 2014; L. Kawinwanichakij et al. 2021; A. George et al. 2024, 2025), our sample consists exclusively of QGs above this threshold (see Section 2).

Following Paper II, we model the SMR of massive QGs by fitting a linear relation (Eq. 2) using the Bayesian regression tool LINMIX.[14] This package employs a Markov Chain Monte Carlo approach to estimate the posterior distributions of the best-fitting parameters, R_0 and α. An advantage of LINMIX is that it accounts for measurement uncertainties in both stellar mass and effective radius during the fitting process.

In this work, for the first time, we investigate the SMRs for bulge and disk components of SFGs and QGs

[14] https://linmix.readthedocs.io/en/latest/src/linmix.html

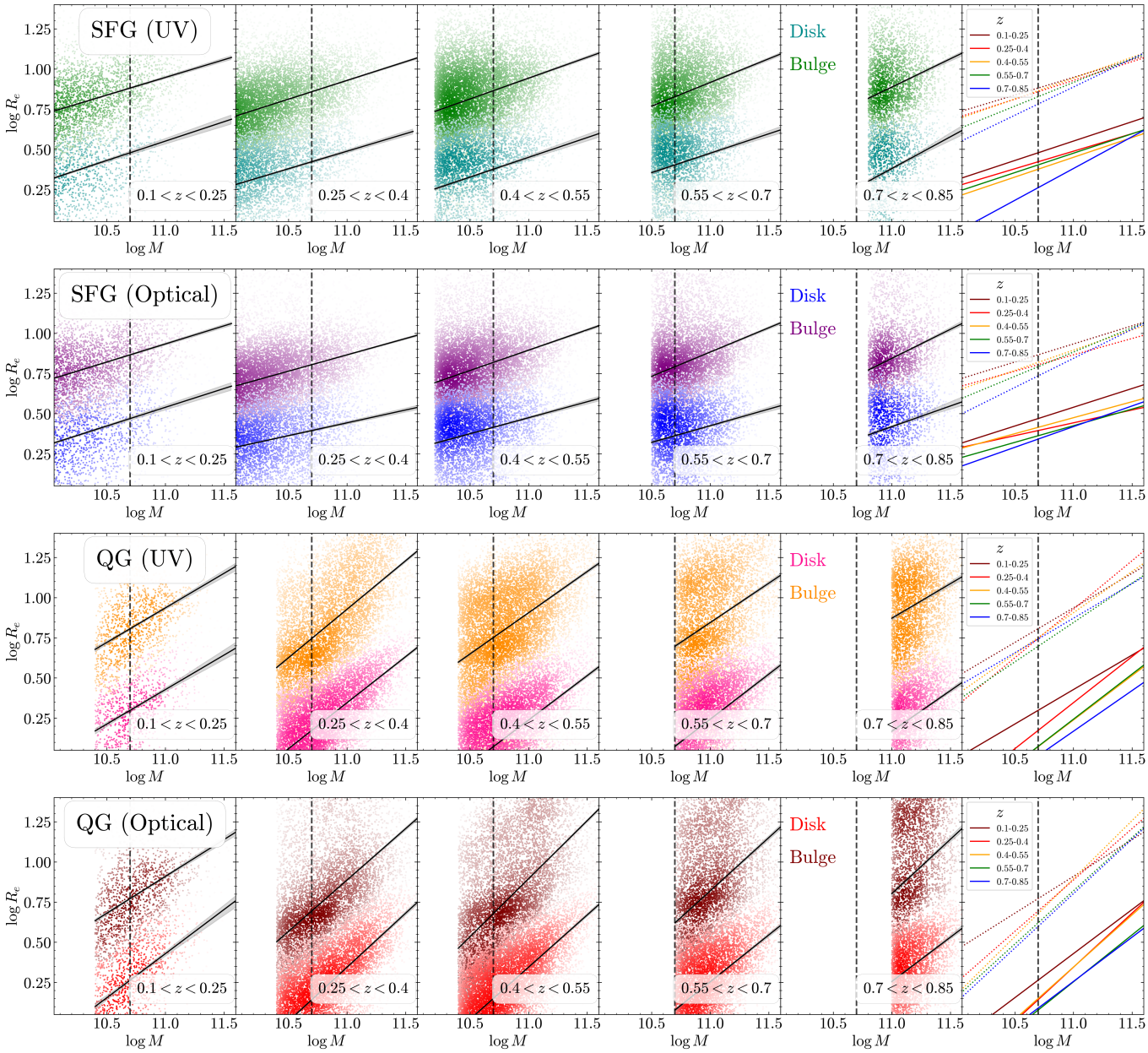

Figure 4. The SMRs for bulges and disks of SFGs (two rows on top) and QGs (two rows on the bottom). For SFGs and QGs, the first row shows the SMR in rest-UV and the second row shows the same in rest-optical. In each row, the first five panels show the SMRs in different redshift bins with the best-fit SMRs for the components are shown in black and uncertainty in gray band. In each redshift bin, the distribution of bulges and disks in the SMR plane is shown in separate colors as labeled in the image and we follow the same color pattern throughout this work. The final column illustrates the best-fit SMRs from all redshift bins together (solid lines for disks and dotted lines for bulges). In every panel, the vertical dashed line denotes the fiducial mass $M_0 = 5 \times 10^{10} M_\odot$.

separately in the rest-UV and rest-optical wavelengths. Based on our simulations, we restrict the SMR analysis of structural components to bulges with $B/T > 0.2$ and disks with $B/T < 0.8$. This is because unless a component contributes at least 20% of the total light of a galaxy, we are unable to reliably fit its Sérsic profile (Section 4).

We use the total stellar masses of galaxies (instead of their component stellar masses) to fit the SMRs for galaxy bulges and disks. While a multi-wavelength decomposition in the IR would ideally allow for individual component mass estimates, such an approach is precluded by the limited angular resolution of the IR data, which is up to three times coarser than that of the

Table 2. Best-fit parameters of the SMR (Eq. 2) and the size evolution (Eq. 3) of the bulge and disk components of SFGs and QGs in rest-frame UV and optical wavelengths.

Type	Comp.	z	$\log R_0$	α	$\sigma_{\log R_e}$	$\log M_l$	N_t	N_s	z_{med}	R_e^0	β
					3000Å						
SFG	Bulge	$0.10-0.25$	0.48 ± 0.01	0.24 ± 0.02	0.16 ± 0.00	9.7	4671	1909	0.21	3.68 ± 0.67	-1.09 ± 0.45
		$0.25-0.40$	0.42 ± 0.01	0.22 ± 0.01	0.20 ± 0.00	9.7	15196	6098	0.31		
		$0.40-0.55$	0.38 ± 0.01	0.25 ± 0.02	0.22 ± 0.00	10.2	10971	3750	0.44		
		$0.55-0.70$	0.40 ± 0.01	0.24 ± 0.02	0.21 ± 0.00	10.5	7947	3471	0.63		
		$0.70-0.85$	0.26 ± 0.02	0.39 ± 0.05	0.23 ± 0.00	10.8	3460	1426	0.74		
	Disk	$0.10-0.25$	0.88 ± 0.01	0.22 ± 0.01	0.17 ± 0.00	9.7	4671	4581	0.20	8.50 ± 0.64	-0.53 ± 0.19
		$0.25-0.40$	0.86 ± 0.00	0.23 ± 0.00	0.17 ± 0.00	9.7	15196	15009	0.31		
		$0.40-0.55$	0.87 ± 0.00	0.26 ± 0.01	0.19 ± 0.00	10.2	10971	10878	0.45		
		$0.55-0.70$	0.83 ± 0.00	0.29 ± 0.01	0.19 ± 0.00	10.5	7947	7883	0.63		
		$0.70-0.85$	0.78 ± 0.01	0.35 ± 0.02	0.19 ± 0.00	10.8	3460	3444	0.74		
QG	Bulge	$0.10-0.25$	0.30 ± 0.01	0.43 ± 0.04	0.14 ± 0.00	10.4	1403	990	0.19	2.40 ± 0.35	-1.51 ± 0.35
		$0.25-0.40$	0.17 ± 0.00	0.57 ± 0.01	0.14 ± 0.00	10.4	9092	7630	0.35		
		$0.40-0.55$	0.07 ± 0.00	0.55 ± 0.01	0.19 ± 0.00	10.4	11485	8295	0.46		
		$0.55-0.70$	0.07 ± 0.01	0.56 ± 0.02	0.27 ± 0.00	10.7	7146	5605	0.65		
		$0.70-0.85$	0.02 ± 0.02	0.50 ± 0.03	0.22 ± 0.00	11.0	4193	3144	0.76		
	Disk	$0.10-0.25$	0.81 ± 0.01	0.43 ± 0.03	0.16 ± 0.00	10.4	1403	1346	0.18	6.76 ± 0.79	-0.49 ± 0.29
		$0.25-0.40$	0.75 ± 0.00	0.60 ± 0.01	0.17 ± 0.00	10.4	9092	8822	0.35		
		$0.40-0.55$	0.75 ± 0.00	0.51 ± 0.01	0.21 ± 0.00	10.4	11485	11308	0.46		
		$0.55-0.70$	0.70 ± 0.01	0.49 ± 0.02	0.27 ± 0.00	10.7	7146	6945	0.64		
		$0.70-0.85$	0.74 ± 0.02	0.43 ± 0.04	0.24 ± 0.00	11.0	4193	4176	0.76		
					5000Å						
SFG	Bulge	$0.10-0.25$	0.47 ± 0.01	0.23 ± 0.02	0.18 ± 0.00	9.7	5220	2305	0.20	3.24 ± 0.34	-0.70 ± 0.26
		$0.25-0.40$	0.40 ± 0.01	0.16 ± 0.01	0.19 ± 0.00	9.7	15183	7348	0.31		
		$0.40-0.55$	0.41 ± 0.01	0.20 ± 0.02	0.19 ± 0.00	10.2	10923	5443	0.45		
		$0.55-0.70$	0.36 ± 0.00	0.21 ± 0.02	0.21 ± 0.00	10.5	7839	4438	0.63		
		$0.70-0.85$	0.34 ± 0.02	0.26 ± 0.05	0.18 ± 0.00	10.8	3176	1842	0.74		
	Disk	$0.10-0.25$	0.87 ± 0.00	0.22 ± 0.01	0.18 ± 0.00	9.7	5220	5091	0.20	8.08 ± 0.80	-0.64 ± 0.25
		$0.25-0.40$	0.80 ± 0.00	0.20 ± 0.00	0.16 ± 0.00	9.7	15183	14817	0.31		
		$0.40-0.55$	0.82 ± 0.00	0.25 ± 0.01	0.16 ± 0.00	10.2	10923	10704	0.45		
		$0.55-0.70$	0.79 ± 0.00	0.30 ± 0.01	0.17 ± 0.00	10.5	7839	7661	0.63		
		$0.70-0.85$	0.73 ± 0.01	0.36 ± 0.02	0.16 ± 0.00	10.8	3176	3101	0.74		
QG	Bulge	$0.10-0.25$	0.26 ± 0.01	0.54 ± 0.04	0.22 ± 0.00	10.4	1622	1268	0.18	2.07 ± 0.29	-1.02 ± 0.34
		$0.25-0.40$	0.14 ± 0.00	0.67 ± 0.01	0.24 ± 0.00	10.4	9131	8502	0.35		
		$0.40-0.55$	0.15 ± 0.00	0.65 ± 0.01	0.23 ± 0.00	10.4	11577	10442	0.46		
		$0.55-0.70$	0.08 ± 0.01	0.58 ± 0.02	0.26 ± 0.00	10.7	7196	6572	0.64		
		$0.70-0.85$	0.09 ± 0.02	0.55 ± 0.04	0.22 ± 0.00	11.0	3944	3631	0.76		
	Disk	$0.10-0.25$	0.77 ± 0.01	0.46 ± 0.02	0.16 ± 0.00	10.4	1622	1455	0.18	6.87 ± 0.39	-0.99 ± 0.14
		$0.25-0.40$	0.69 ± 0.00	0.64 ± 0.01	0.19 ± 0.00	10.4	9131	7414	0.35		
		$0.40-0.55$	0.68 ± 0.00	0.72 ± 0.01	0.23 ± 0.00	10.4	11577	10247	0.46		
		$0.55-0.70$	0.62 ± 0.01	0.66 ± 0.02	0.30 ± 0.00	10.7	7196	6273	0.64		
		$0.70-0.85$	0.60 ± 0.03	0.68 ± 0.06	0.31 ± 0.00	11.0	3944	3510	0.76		

NOTE—The column $\log M_l$ refers to the mass completeness cut in $\log M$. N_t refers to the total number of galaxies in the mass-complete sample with successful SE++ fits in a given redshift bin, while N_s is the number of galaxies used for the SMR fits ($B/T > 0.2$ for bulges and $B/T < 0.8$ for disks). The uncertainties below 0.005 are simply shown as 0.00. The uncertainties in z_{med} (median z) are all below 0.005.

CLAUDS+HSC imaging. Furthermore, structural parameters vary significantly with wavelength (Section 4). Hence, by adopting total stellar mass, we avoid assigning parameters from the optical light profile decomposition to the (unresolved) IR components of the spectral energy distribution (SED) fitting. This approach ensures a robust and uniform baseline for our analysis across the entire redshift range. Although this differs from the component-mass approach utilized in some of the similar works in the literature (e.g., A. Hashemizadeh et al. 2022; A. S. G. Robotham et al. 2022a), it enables a more direct investigation into how the internal components of galaxies with similar stellar mass have evolved in size since $z \sim 0.85$.

We present the best-fit SMRs for the bulge and disk components of SFGs and QGs in Figure 4, with the corresponding best-fit parameters provided in Table 2. In each row, the first five panels display the SMRs across

increasingly higher redshift bins, while the final panel overlays the SMRs from all bins to facilitate comparison. The top two rows show the component SMRs for SFGs in the rest-frame UV and optical, respectively, while the bottom two rows provide the same for the QG population.

For both SFGs and QGs, bulges are consistently more compact than their companion disks across both rest-frame wavelengths. This size offset is more pronounced in the rest-UV than in the optical, driven by the more extended nature of disks and the increased compactness of bulges at shorter wavelengths. In addition to redshift evolution in the SMR slopes, the normalization at the fiducial mass (M_0 is indicated by the vertical dashed line) decreases at higher redshifts. This confirms that, at fixed total stellar mass, both galaxy components were significantly more compact in the past.

Figure 5 shows the best-fit SMR parameters (filled symbols) and their evolution with redshift for both SFGs and QGs. As expected, at a given fiducial stellar mass, disks in both SFGs and QGs have larger characteristic sizes (i.e., higher SMR zero points) than bulges, in both rest-frame UV and optical wavelengths (top row of Figure 5). This size difference between disks and bulges is more pronounced in the bluer band. For example, at $0.4 < z < 0.55$, the disk of a fiducial SFG (QG) is 1.57 (2.39) times larger than the corresponding bulge in the rest-frame optical. In the rest-frame UV, this difference increases: the disk is 2.09 (3.79) times more extended than the bulge in a similar SFG (QG).

Regardless of the wavelength, the sizes of bulges and disks are larger for SFGs than for QGs. For example, the bulges (disks) of 5×10^{10} $M_\odot$ SFGs are $62 - 91\%$ $(26 - 48\%)$ larger than those of QGs with the same fiducial mass in all redshift bins at 5000Å. P. Lang et al. (2014) also report that the bulges and disks in $\log M \sim 10.5$ SFGs are more extended than those in similar QGs, although this offset is a factor of ~ 1.5 in a much broader redshift interval ($0.5 < z < 2.5$).

We also compare the evolution in the parameters of the SMR for galaxy bulge and disk components to the equivalent evolution of the SMR parameters for galaxies fitted with a single Sérsic index (open circles in Figure 5; Paper I). The zero points of galaxy disks are larger than the SMR zero points from the single Sérsic component measurements. In contrast, bulges are much more compact than the total size of their host galaxies, in line with other studies (e.g., L. Costantin et al. 2021). However, for SFGs, the total galaxy size (from single-component fit) closely resembles those of disk sizes, although the offset between them increases with cosmic time. On the other hand, the sizes of bulges and disks for QGs are very different from the single-component size measurements.

The top row in Figure 5 show a clear evidence for evolution in the zero point of the SMR — i.e., the characteristic size of bulges and disks at a fixed fiducial stellar mass. Both bulges and disks exhibit size growth over cosmic time. Between the redshift bins $0.7 < z < 0.85$ and $0.1 < z < 0.25$, the bulges of fiducial SFGs (QGs) increase in size by 66% (91%) in the rest-frame UV, and by 35% (48%) in the rest-frame optical wavelength. Similarly, the disks of fiducial SFGs (QGs) grow by 26% (17%) in the UV, and by 38% (48%) in the optical wavelength. These results highlight two key trends: (1) bulge sizes evolve more rapidly than disk sizes in the rest-frame UV light, and (2) the rate of size growth is wavelength-dependent. We explore these trends further in Section 6.

The SMR slopes are steeper for QGs than for SFGs in both wavelengths (middle row in Figure 5). The slopes range from 0.16 to 0.36 for SFGs, while they are notably steeper $(0.43 - 0.72)$ for QGs. P. Dimauro et al. (2019) also report similar SMR slopes for SFG disks and QG bulges at these redshifts. The slopes we find for the SFG components also agree with K. V. Nedkova et al. (2024), but these authors report steeper slopes for the QG bulges and shallower slopes for the QG disks. We note that both of these works (P. Dimauro et al. 2019; K. V. Nedkova et al. 2024) adopt the component mass (instead of the total mass) in the SMR analysis.

In addition, the SMR relation tend to steepen for SFG bulges and disks with redshift, a trend not observed for SFG SMRs from single/global Sérsic profiles in this redshift range (e.g., A. van der Wel et al. 2014; L. Kawinwanichakij et al. 2021; A. George et al. 2024). In contrast, if we exclude the lowest redshift bin where our sample size is the lowest, we find a decreasing trend in the slopes for QG bulges (in UV and optical) and disks (in UV). This is again different from the global SMR trends reported in the literature (A. van der Wel et al. 2014; L. A. Mowla et al. 2019; L. Kawinwanichakij et al. 2021; K. V. Nedkova et al. 2021; A. George et al. 2024, 2025).

The intrinsic scatter in the SMR, denoted by $\sigma_{\log R_e}$, is generally lower for the structural components (bulges and disks) than for the global SMR of SFGs (left panels in the bottom row of Figure 5). In contrast, QGs show a comparable level of scatter between their global SMR and the SMRs of their individual components, except for their bulges in rest-UV (right panels). Overall, SFG disk sizes exhibit a tighter correlation with stellar mass than their bulge sizes across both wavelengths, as reflected by the lower intrinsic scatter in their SMR. In contrast,

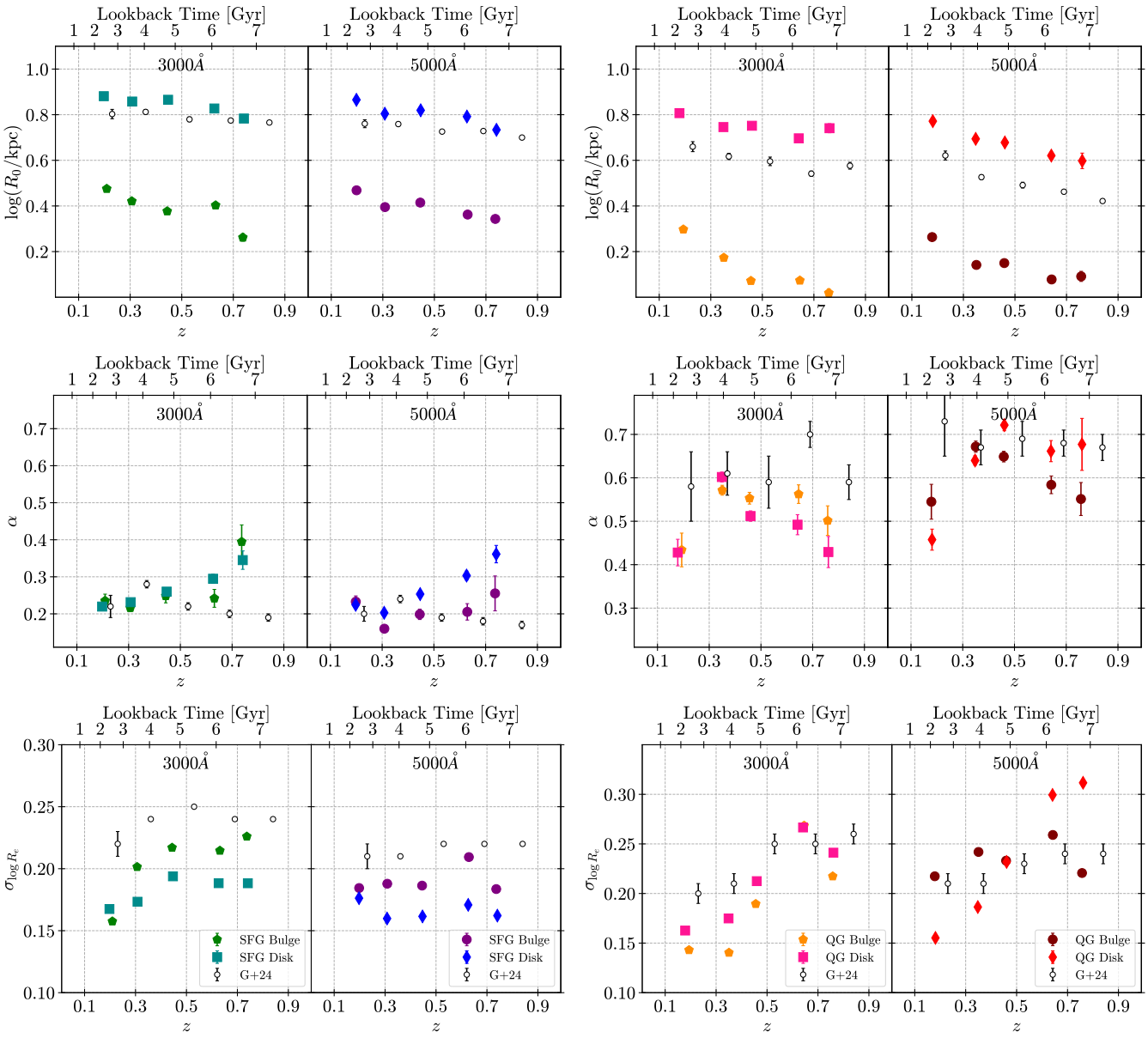

Figure 5. Redshift evolution of the best-fit SMR parameters for SFGs (left) and QGs (right). We plot the results in rest-UV and rest-optical for SFGs and QGs in separate sub-panels. Within each sub-panel, we show the SMR parameters for bulge and disk components separately. We also show the global SMR parameters based on the single Sérsic profile fitting from A. George et al. (2024, G+24) as open circles. Top row: Evolution of the SMR zero points ($\log R_0$). Middle row: Evolution of the SMR slopes ($\alpha = \mathrm{d}\log R_e/\mathrm{d}\log M$). Bottom row: Evolution of the intrinsic scatter in the SMR ($\sigma_{\log R_e}$).

QG bulges show smaller scatter than their disks in the rest-UV, whereas no such clear distinction exists in the rest-optical.

On average, the intrinsic scatter for SFG components ranges from 0.16 to 0.23, while for QG components it spans a broader range, from 0.14 to 0.31. For SFG disks, this scatter remains remarkably stable across the sampled redshift range, suggesting that disk growth is governed by well-regulated physical processes, such as continuous star formation and gas accretion. In contrast, the increasing scatter observed with redshift for SFG bulges (in rest-UV) and QG components (except for QG bulges in rest-optical) likely reflects a higher degree of structural diversity or more stochastic assembly histories at earlier epochs. The lack of evolution in the SMR scatter for optical QG bulges implies that the distribution of old stellar population in them may be also driven by well regulated processes, just like SFG components. Finally, the total range of intrinsic scatter we observe for bulge and disk components ($0.14 - 0.31$) is

broadly consistent with the scatter found for the global SMRs of SFGs and QGs in Paper I, indicating that the stochasticity in component growth mirrors that of the galaxy as a whole.

In summary, our multi-wavelength analysis demonstrates that bulges and disks of SFGs and QGs follow distinct scaling relations that vary in slope, scatter, and wavelength-dependence. These systematic differences suggest that the internal components of both SFGs and QGs have been shaped by different physical assembly processes since $z \sim 0.85$. By establishing these robust relations at each epoch, we can now isolate the redshift evolution of component sizes at a fixed galaxy stellar mass to explore the physical mechanisms driving their growth.

6. SIZE EVOLUTION OF BULGES AND DISKS

We investigate the evolution of the structural components of galaxies as the Universe ages by tracking their characteristic sizes at a fiducial stellar mass of 5×10^{10} $M_\odot$, derived from their respective SMRs. We use SMR-based characteristic sizes because they are less biased than simple median sizes within stellar mass bins; the SMR fitting process explicitly accounts for measurement uncertainties in both size and stellar mass. We model this redshift evolution in two rest-frame wavelengths (3000Å and 5000Å) using a power-law model,

$$R_e = R_e^0 (1+z)^\beta, \tag{3}$$

where R_e^0 is the characteristic size of a structural component of galaxies at $z = 0$.

As we describe in Section 5, the characteristic sizes of the bulge components are based on galaxies with $B/T > 0.2$ and the sizes of the disk components are based on galaxies with $B/T < 0.8$, to ensure the reliability of the component size measurements. Because of this, the number of galaxies used to fit the SMRs and, subsequently, the size evolution curve for the bulge and disk components are not the same. We provide the best-fit parameters in Table 2 and display the main results in Figure 6.

Consistent with our SMR analysis (Section 5), Figure 6 shows that disks (cyan/blue curves for SFGs and pink/red for QGs) are systematically more extended than the global galaxy size (black curves) across both rest-frame wavelengths, while bulges (green/purple curves for SFGs and orange/maroon for QGs) remain the most compact components.

Notably, we find that structural components grow at different rates than the galaxy as a whole (the left panel of Figure 6). For instance, the increasing offset between the sizes of SFG disks (blue/cyan) and global sizes (black) over cosmic time in the left panel implies that disks expand more rapidly than the total galaxy profile ($\beta = -0.53 \pm 0.19$ vs $\beta = -0.26 \pm 0.13$ in UV; $\beta = -0.64 \pm 0.25$ vs $\beta = -0.35 \pm 0.14$ in optical). SFG bulges (green/purple) exhibit even steeper evolution, particularly in the rest-UV ($\beta = -1.09 \pm 0.45$ in UV; $\beta = -0.70 \pm 0.26$ in optical), suggesting they play a significant role in the structural transformation of star-forming systems. While these growth rates are subject to uncertainties, the trend of faster disk growth in the longer wavelength — contrasted with the opposite behavior in bulges — further underscores the distinct assembly histories of these two components.

In contrast, the evolutionary tracks for QG disks (pink/red curves in the right panel of Figure 6) exhibit markedly different behavior. Their sizes remain significantly larger than both the global sizes of QGs (black curves) and the sizes of QG bulges (orange/maroon curves). Although QG bulges grow rapidly with time, the growth rate of their disks — unlike in SFGs — is comparable to that of their global sizes. These highlight key structural differences in how SFGs and QGs grow over cosmic time.

While we compare the global size evolution from Paper I with the component sizes derived in this work, we caution the reader that these samples are not strictly identical. Specifically, the galaxy populations contributing to the global curves (black) and the component curves (colored) in Figure 6 differ in their selection criteria. Furthermore, the sub-samples used for bulge and disk evolution differ from one another (see Section 4 and Table 1). Consequently, the global size evolution is not a simple superposition of the bulge and disk evolutionary tracks, particularly for SFGs where selection effects significantly impact the composition of the bulge and disk samples.

As noted in Section 5, the pace of structural evolution exhibits a clear wavelength dependence. For both SFGs and QGs, bulge components show more rapid expansion in the rest-UV than in the optical; specifically, between $z = 0.85$ and $z = 0.1$ (~ 6 Gyr), QG (SFG) bulges grew by 120% (98%) in the UV compared to a more modest 76% (44%) in the optical. Conversely, disk growth in QGs is more pronounced in the optical (68%) than in the UV (29%). Notably, SFG disks show no significant difference between their UV (32%) and optical (40%) growth rates. This suggests that while bulge and quiescent disk evolution are sensitive to wavelength-dependent stellar population gradients, SFG disks likely grow through more spatially uniform, continuous star formation across the sampled wavelengths.

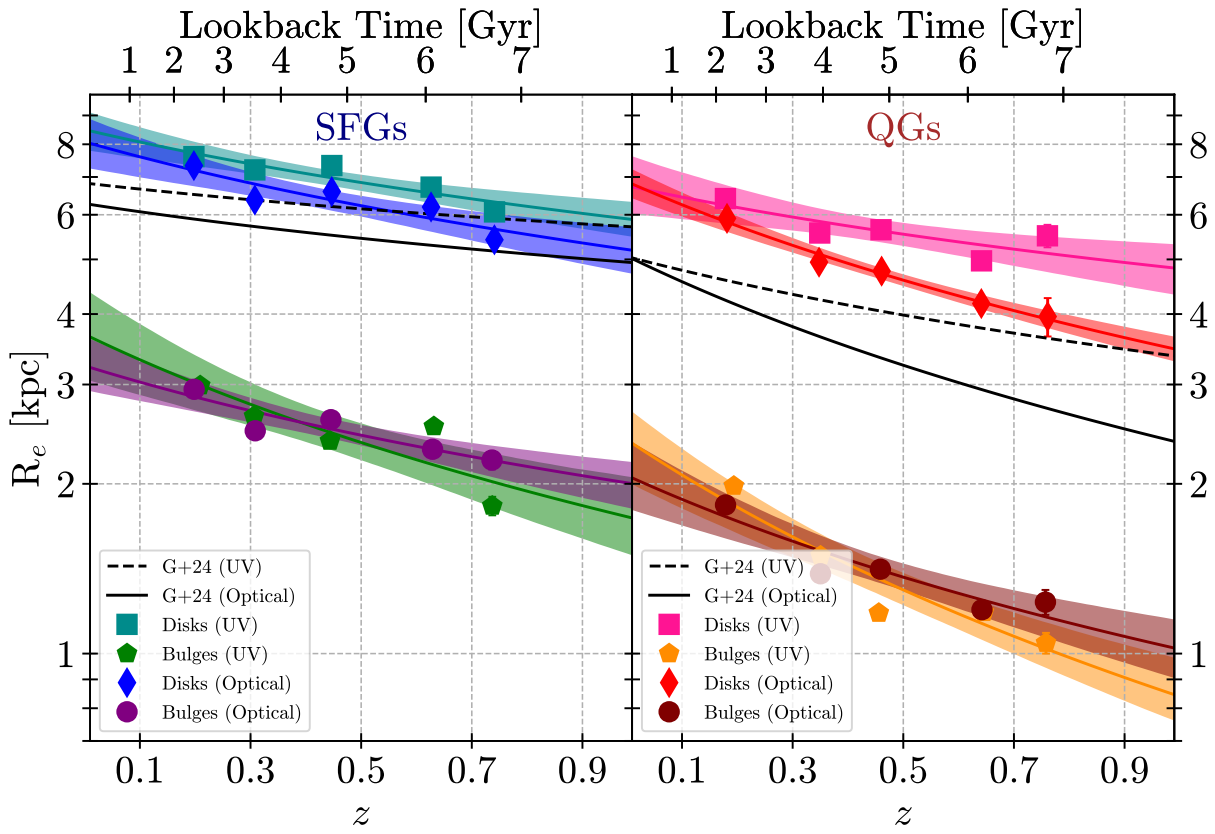

Figure 6. Left: Redshift evolution of characteristic sizes of SFG bulges and disks in the rest-frame UV (3000Å) and optical (5000Å) wavelengths. The global size evolution curves from A. George et al. (2024, G+24) based on single Sérsic profile fitting are shown in black. Right: Redshift evolution of characteristic sizes of QG bulges and disks in two rest-frame wavelengths.

Finally, for both SFGs and QGs, bulges exhibit a faster rate of size growth compared to disks. This trend is consistent with recent findings by K. V. Nedkova et al. (2024), who also reported more rapid growth in the characteristic sizes of bulges relative to disks based on the Hubble Frontier Fields and CANDELS data. In our analysis, we further find that this difference in growth rates between bulges and disks is wavelength-dependent. Specifically, the disparity is more pronounced at rest-frame 3000Å than at 5000Å: Growth curve is 105% (208%) steeper for SFG (QG) bulges than their disks in rest-UV, but the difference is negligible — 9% (3%) — in rest-optical.Thus, the UV light more clearly reveals the differential size evolution between galaxy components than optical light.

Synthesizing these trends, we find that the structural growth is fundamentally coupled to both the specific galaxy component and the observed wavelength. Figure 7 presents a schematic of an average two-component SFG (left) and QG (right) with a fiducial stellar mass $\log M \sim 10.7$ at $z \sim 0.5$. The disks of both SFGs and QGs appear more extended in rest-frame UV light compared to the optical light. Meanwhile, the bulges are slightly larger, if not the same, in the optical than in the UV. Moreover, the difference between the UV sizes of bulges and disks is more pronounced in QGs than in SFGs. These wavelength-dependent differences in the sizes along with the differences in their redshift evolution (Figure 6) highlight the distinct physical processes shaping bulges and disks, and underscore the role of stellar population gradients and structural growth in galaxy morphological evolution.

7. DRIVERS OF BULGE AND DISK SIZE EVOLUTION

Our bulge+disk decomposition of the CLAUDS+HSC galaxies across two rest-frame wavelengths confirms that bulges are significantly more compact than their companion disks and, crucially, reveals that these structural components follow distinct evolutionary pathways. Beyond the wavelength-dependence of the sizes themselves, the pace of structural evolution also varies with wavelength and galaxy type (Section 6). These nuances suggest that while certain global trends persist for all bulges and disks, their specific growth trajectories are heavily influenced by the star-formation activity of the host

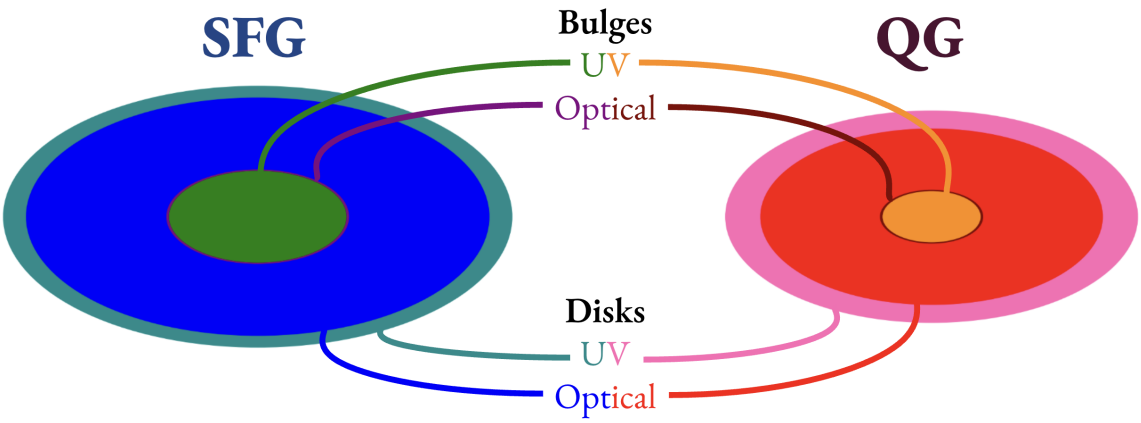

Figure 7. A simple model of an average SFG (left) and QG (right) with a fiducial stellar mass $\log M \sim 10.7$ at $z = 0.5$. The sizes of the disks and bulges are shown to scale relative to each other. Disks appear more extended in the rest-UV (cyan/pink) than in the rest-optical (blue/red), whereas bulges are more compact in the UV (green/orange) compared to the optical (purple/maroon). Additionally, both bulges and disks are smaller in QGs than in SFGs. For comparison, a constant axis ratio (q) is adopted for both galaxy types.

galaxy. Such divergence warrants a separate examination of the physical mechanisms driving the structural evolution of the star-forming and quiescent populations.

7.1. *Star-forming Galaxies*

The simple schematic picture of an SFG with the fiducial mass observed in the multi-wavelength analysis using bulge+disk decomposition (Figure 7) and the trends observed in the evolution of structural parameters (the left panel of Figure 6) support the evolutionary scenario proposed in our Paper I. There, we concluded that the observed overall size evolution of the SFGs (from single-component Sérsic fits at two rest-frame wavelengths) must be shaped by the growth of bulges within them. The fast size growth of bulges that we observe in this work provide additional arguments for our earlier interpretation.

Bulges are centrally concentrated stellar distributions in galaxies, that become prominent in galaxies with decreasing redshift (M. Martig et al. 2009; S. Sachdeva 2013; P. Lang et al. 2014; S. Sachdeva et al. 2017; S. Tacchella et al. 2019; A. George et al. 2024). There are several physical mechanisms that can drive their formation and growth. Classical bulges, which exhibit properties similar to early-type galaxies, can initially form through the dissipative collapse of protogalactic gas clouds (O. J. Eggen et al. 1962) or the coalescence of giant clumps in primordial disks (e.g., F. Bournaud et al. 2007; N. M. Förster Schreiber & S. Wuyts 2020). These structures can subsequently grow through secular disk instabilities (G. De Lucia et al. 2011) or hierarchical galaxy mergers (P. F. Hopkins et al. 2010a; A. Brooks & C. Christensen 2016).

Galaxy mergers are thought to play a crucial role in the growth of bulges in galaxies. Though major mergers can form central bulges and form/reform disks around them from the surviving material (J. E. Barnes & L. Hernquist 1992, 1996; V. Springel & L. Hernquist 2005; T. Naab et al. 2006; P. F. Hopkins et al. 2009), such mergers may not have played a crucial role in bulge formation/growth in the last 7 billion years due to their low frequency (C. J. Conselice et al. 2003, 2022; C. López-Sanjuan et al. 2009, 2010; J. M. Lotz et al. 2011; S. Kaviraj et al. 2014; N. Thibert et al. 2021; Q. Duan et al. 2025). However, during this epoch, minor mergers are frequent (J. M. Lotz et al. 2011) and can significantly facilitate bulge growth through the redistribution of mass and angular momentum. In these events, the satellite galaxy is disrupted by tidal forces, with its stellar and gaseous content sinking toward the potential well of the host via dynamical friction (M. Steinmetz & J. F. Navarro 2002; L. Oser et al. 2010). Simultaneously, the gravitational interaction kinematically heats the host disk, scattering stars from ordered circular orbits into the random, pressure-supported orbits characteristic of a bulge component (T. J. Cox et al. 2008; P. F. Hopkins et al. 2010b). This combination of direct satellite accretion and the dynamical restructuring of the host disk provides a robust mechanism for the continuous assembly of bulges since $z \sim 0.85$.

Bulges can also grow through internal (secular) processes, which differ from merger-driven growth in both their timescale and dynamical nature. Unlike the violent kinematic heating caused by mergers, secular evolution is a gradual process where internal disk instabilities —

such as bars or spiral arms — redistribute angular momentum within the disk plane (E. Athanassoula 2005; J. A. Sellwood 2014). These structures funnel gas and stars toward the center without destroying the disk's underlying rotational support, allowing mass to settle into a more stable, centrally concentrated configuration (J. Kormendy & D. B. Fisher 2008; L. Zhang et al. 2025). The resulting pseudobulges retain disk-like kinematics and nearly exponential light profiles, distinguishing them from the pressure-supported classical bulges formed through external interactions (J. Kormendy & R. C. Kennicutt 2004; D. B. Fisher & N. Drory 2011; J. Hu et al. 2024).

Regardless of the underlying growth mechanism, the emergence of a bulge fundamentally modulates both the structural morphology and the subsequent evolutionary trajectory of the host galaxy. Due to their high central stellar mass densities and compact profiles, bulges shift the global light distribution toward more concentrated states, effectively reducing the measured global effective radius. Beyond these geometric alterations, the development of a substantial central mass component can kinematically stabilize the surrounding gas disk against gravitational fragmentation (M. Martig et al. 2009). This stabilization regulates the efficiency of star formation by increasing the marginal stability of the disk, suggesting that bulge assembly is a primary driver in steering a galaxy's progression along the star-forming sequence toward eventual quiescence.

Building on our earlier results from Paper I, we proposed two main scenarios for bulge growth in SFGs. In Scenario I, both the bulge and the disk grow concurrently as the SFG evolves. In Scenario II, the bulge alone grows, and this growth pushes the active star-forming regions farther out in the disk. We can probe these two scenarios in more detail with the results from our multi-wavelength bulge+disk decomposition.

Our results show that SFG disks are consistently more extended in the rest-UV than in the optical, with both radii increasing over cosmic time (Figure 6). While the larger rest-UV sizes are indicative of inside-out growth — where younger stellar populations are preferentially located in the disk outskirts — this observation is consistent with both scenarios. The primary differentiator is the evolution of the bulge-to-total (B/T) ratio, which remains relatively stable across our redshift range. Although the B/T ratio is inherently more difficult to constrain than the effective radius due to the degeneracies in light-profile modeling (Section 4), the lack of significant B/T evolution suggests that the disk is also growing concurrently. This indicates that while bulges expand in physical size more rapidly than disks, their relative light contribution remains relatively steady, providing the strongest evidence for the concurrent growth described in Scenario I.

Furthermore, the sizes of SFG disks grow faster than the total (single Sérsic) sizes of SFGs themselves in both rest-frame wavelengths (the left panel of Figure 6). The total sizes of SFGs and the sizes of their disks are very similar in the highest redshift bin, but the total sizes of SFGs deviate significantly from the disk size with decreasing redshift. The observed deceleration in the growth of global sizes of the SFGs at $z < 1$ from our pilot study must be driven by the size growth of bulges. In fact, the growth rate of disks in rest-optical ($\beta = -0.64 \pm 0.24$) we find here is consistent with the fast growth of SFGs reported at higher redshifts by R. J. Williams et al. (2010, $\beta = -0.77$ at $0.5 < z < 2$) and A. van der Wel et al. (2014, $\beta = -0.75$ at $0 < z < 3$), supporting our hypothesis. This demonstrates that while the physical growth of the disk component remains rapid and consistent with high-redshift trends, the apparent deceleration of the global size growth is a measurement effect driven by the increasing influence of the compact bulge on the single-Sérsic fit. Specifically, as the bulge becomes a more structurally distinct feature at lower redshifts, it increases the global Sérsic index (n) of the galaxy; this sharpens the central light profile and anchors the global R_e to smaller values, effectively masking the true extent of the disk's expansion.

The size growth of the SFG disks is slightly faster in the longer wavelength ($\beta = -0.64 \pm 0.24$) than in the shorter wavelength ($\beta = -0.53 \pm 0.19$). Although within uncertainties, this small difference in the growth rate could indicate that the star-forming activity in disks may be slowing down as the SFGs evolve. In such a scenario, we would expect a slower size growth in rest-UV than in rest-optical, as observations suggest.

This gradual decline in the star-formation activity of SFGs over cosmic time can be linked to the growth of their internal bulges. By kinematically stabilizing the surrounding gas disk, the galactic bulges can suppress the star formation efficiency, a process known as morphological quenching (M. Martig et al. 2009; A. Saintonge et al. 2012; S. Sachdeva et al. 2017; A. Hashemizadeh et al. 2022). This interpretation is consistent with the observed decline in the specific star formation rate (sSFR) with increasing stellar mass surface density within the central 1 kpc radius (Σ_1 in units of $M_\odot/\mathrm{kpc}^2$; Paper I). As bulge growth drives Σ_1 towards a threshold value ($\log \Sigma_1 \sim 9$), the sSFR begins to decrease via inside-out suppression of star formation (K. E. Whitaker et al. 2017; A. George et al. 2024). Further bulge growth can eventually quench a galaxy; galaxies with very high

central mass density ($\log \Sigma_1 \gtrsim 9.7$) are generally quiescent (K. E. Whitaker et al. 2017; K. A. Suess et al. 2021; V. Estrada-Carpenter et al. 2023; A. George et al. 2024). The physical evidence for this process is also reflected in our finding that B/T values are higher in the optical than in the UV (Figure 3).

However, we observe that bulges grow faster in UV, suggesting an ongoing addition of UV-bright material. Since we model bulges with a free Sérsic index, the fits may include other non-disk components, such as stellar halos. Hence, our bulge measurements may include material accreted through minor mergers, which tend to settle in the outer regions, contributing to halo growth (D. J. Williams et al. 2025). These accreted *ex-situ* stars can be younger and/or lower in metallicity, making them more prominent in the UV and thus boosting UV-measured sizes more than optical ones (I. Saviane et al. 2008; A. P. Cooper et al. 2010; M. Hirschmann et al. 2015).

The gradual increase in the central concentration of bulge components is reflected in the distribution of bulge Sérsic indices (n_B's) in SFGs and their evolution with redshift (upper panel of Figure 8). We find that the Sérsic indices of SFG bulges in the optical light (purple) increase over cosmic time, such that by $z < 0.4$, their profiles in the rest-frame optical approach a de Vaucouleurs profile ($n = 4$), consistent with trends reported by P. Dimauro et al. (2019). This suggests that the structural properties of present-day SFG bulges in the rest-optical resemble those of QG bulges, indicating a gradual morphological transformation of bulges toward early-type characteristics. However, we do not find any significant evolution occurring in the UV light (green), where $n_B \sim 1$. This indicates that the distribution of star-forming regions and/or metal-poor stars within SFG bulges remains exponential over the redshift interval we probe.

In summary, we find strong evidence for the growth of centrally concentrated bulges that play a vital role in the evolution of SFGs since $z < 1$. Although this growth of bulges could be driven by various processes (e.g., *in-situ* star formation, disk instability, mergers, etc.), the process rapidly builds up materials in galaxy center and promotes inside-out quenching.

7.2. *Quiescent Galaxies*

Although general trends in the size evolution of QGs (such as relative sizes of components, their size growth, and wavelength dependence) are similar to those of SFGs, there are some notable differences. The sizes of the disks and bulges of QGs are smaller than those of SFGs (Sections 5 and 6). In addition, the global (single-Sérsic) sizes of QGs are significantly different from the sizes of their individual components. The pace of the size evolution for QG disks is comparable to that of SFGs in the rest-UV. However, the QG disks (in optical) and bulges (in UV and optical) grow at a faster rate than their SFG counterparts.

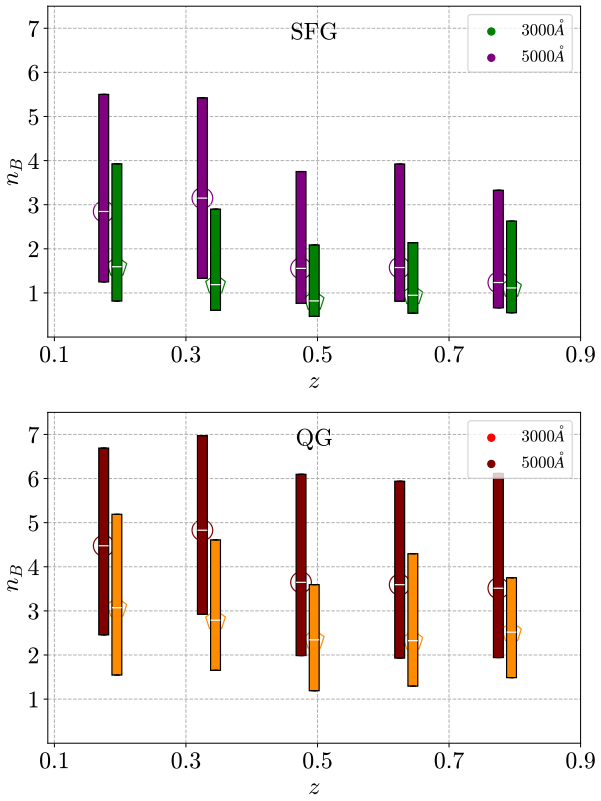

Figure 8. Top: Evolution of Sérsic indices of SFG bulges with stellar mass $10.5 < \log M < 11$ in the rest-UV and in the rest-optical. The colored boxes extend from the first quartile to the third quartile of the Sérsic indices in different redshift bins, with a white horizontal line at the median value. Bottom: Evolution of Sérsic indices of QG bulges with stellar mass $10.5 < \log M < 11$ in the rest-UV and in the rest-optical. Rest of the details are same as in the top panel. We also note that SFG and QG samples are not mass complete at $z > 0.7$ and at $z > 0.55$ respectively.

A significant fraction of QGs retain a disk or a component that can be modeled with an exponential light profile. This is in agreement with previous observational works showing that disk structures exist in many if not all QGs (e.g., P. Dimauro et al. 2019; Q. Cui et al. 2024; K. V. Nedkova et al. 2024; F. Rigamonti et al. 2024). Survival of disks after quenching is also predicted in cosmological simulations. For example, the analysis of galaxy kinematic properties from the EAGLE cosmological simulation shows that when star formation in massive galaxies ($\log M > 10.5$) declines, they trans-

form into spheroids with a disk component (B. Clauwens et al. 2018). These transformations are driven mainly by the accretion of material in the outer halo, allowing disks to survive — albeit in a faded state. By tracing the evolution of the SMR for QG disks in two rest-frame wavelengths, our analysis provides a unique observational probe of how these quenched disks evolve.

Compared to bulges, disks in QGs are not compact (the right panel of Figure 6). Their sizes are comparable to those of the disk components of the SFG population. This similarity in disk sizes between SFGs and QGs could indicate that disk formation in galaxies occurs while they are still active. In Paper I, we find that 20% of the size growth of QGs comes from the progenitor bias driven by newly quenched galaxies (newcomers), a result recently corroborated across both rest-UV and optical wavelengths by M. Pizzardo et al. (2026). Some of the progenitor bias effects should be reflected in the disk profiles, as these newcomer galaxies tend to maintain more prominent and extended disk structures than those quenched at earlier epochs (M. Pizzardo et al. 2026). Additionally, we observe that quiescent disks grow faster in the optical wavelength than in the UV. Thus, if QGs have a disk component, these disks are more extended in UV than in the visible light at higher redshifts, but there is no significant size difference between wavelengths at low redshift due to the slower growth in the UV.

We should also note that, although the disk fades when a galaxy quenches (e.g., D. Christlein & A. I. Zabludoff 2004; C. M. Carollo et al. 2016; J. Matharu et al. 2020; V. Estrada-Carpenter et al. 2023), this fading happens over several hundreds of millions of years. In fact, our rest-frame 3000 Å size measurements are highly sensitive to the age of the stellar population. At this wavelength, the light is dominated by stars formed over the last several hundred million years; specifically, the average flux-weighted age of a simple stellar population with solar metallicity is $\sim$ 300 Myr (G. Bruzual & S. Charlot 2003; D. C. Martin et al. 2005). Thus, the contribution from the newcomers should be more prominent in the rest-UV than in the longer wavelength, as evidenced by the similar UV size evolution slopes (β) observed between SFG and QG disks.

However, QG disks exhibit a significantly higher β in the optical than their SFG counterparts. This accelerated optical growth indicates that QG disks are not merely fading SFG disks; instead, they are subject to cumulative structural assembly via minor mergers that deposit mass into the outskirts. While these mergers can deliver younger/bluer stars — a process that drives the rapid UV growth seen in QG bulges — the overall disk size evolution in the UV is ultimately limited by the rapid fading of these young populations once they are incorporated. Consequently, while the UV light traces the 'memory' of recent star formation in newcomer disks, the optical growth provides a more permanent record of the structural assembly and stellar mass redistribution occurring over longer timescales.

The bulges in QGs are more compact than the SFG bulges (the right panel of Figure 6) and have higher values of n_B (the bottom panel of Figure 8) in both rest-frame wavelengths, indicating that QG bulges have significantly more central concentration. The lack of significant evolution in n_B for QGs with redshift suggests that quenching mechanisms at $z < 1$ are closely coupled with morphological transformation, typically resulting in de Vaucouleurs ($n = 4$) bulges in rest-optical (maroon bars in the bottom panel of Figure 8). While newcomers account for approximately 20% of the population's size growth (Paper I), their inclusion does not shift the median n_B significantly, implying that these galaxies already have significant centrally concentrated profiles when they join the quiescent population.

As galaxies quench and move through the green valley, they undergo significant morphological transformations. In the optical regime, these transitions are characterized by a decrease in R_e and an increase in n, leading to higher stellar mass surface densities without an appreciable increase in total stellar mass (L. Quilley & V. de Lapparent 2022; V. Estrada-Carpenter et al. 2023). However, structural evolution may continue beyond the initial quenching phase. Post-quenching, QGs can become even more centrally concentrated over time, mainly due to the continued accumulation of stellar mass through minor mergers and accretion (e.g., M. Hilz et al. 2013; H. J. Zahid et al. 2019). Even though QG bulges typically do not exhibit de Vaucouleurs profiles in the shorter wavelength (orange bars), their n_B values are consistently higher than those of SFG bulges in the same wavelength, supporting the notion of morphological transformations during and after quenching.

Moreover, the bulges of the quenched galaxies are slightly more compact in UV than in the optical at $z > 0.4$ (the right panel of Figure 6). Although these compact UV bulges could indicate residual star formation in the cores (C. R. Wagner et al. 2015; A. W. S. Man et al. 2016; C. D'Eugenio et al. 2020), galaxy centers are typically older than the galaxy outskirts (K. A. Suess et al. 2019, 2020). Fast processes that form bulges at high z's (e.g., wet compaction) could produce some low-metallicity stars in the centers of galaxy bulges (R. L. Griffith et al. 2011; A. R. Casey & K. C. Schlaufman 2015; S. Lapiner et al. 2023), even though galaxies in

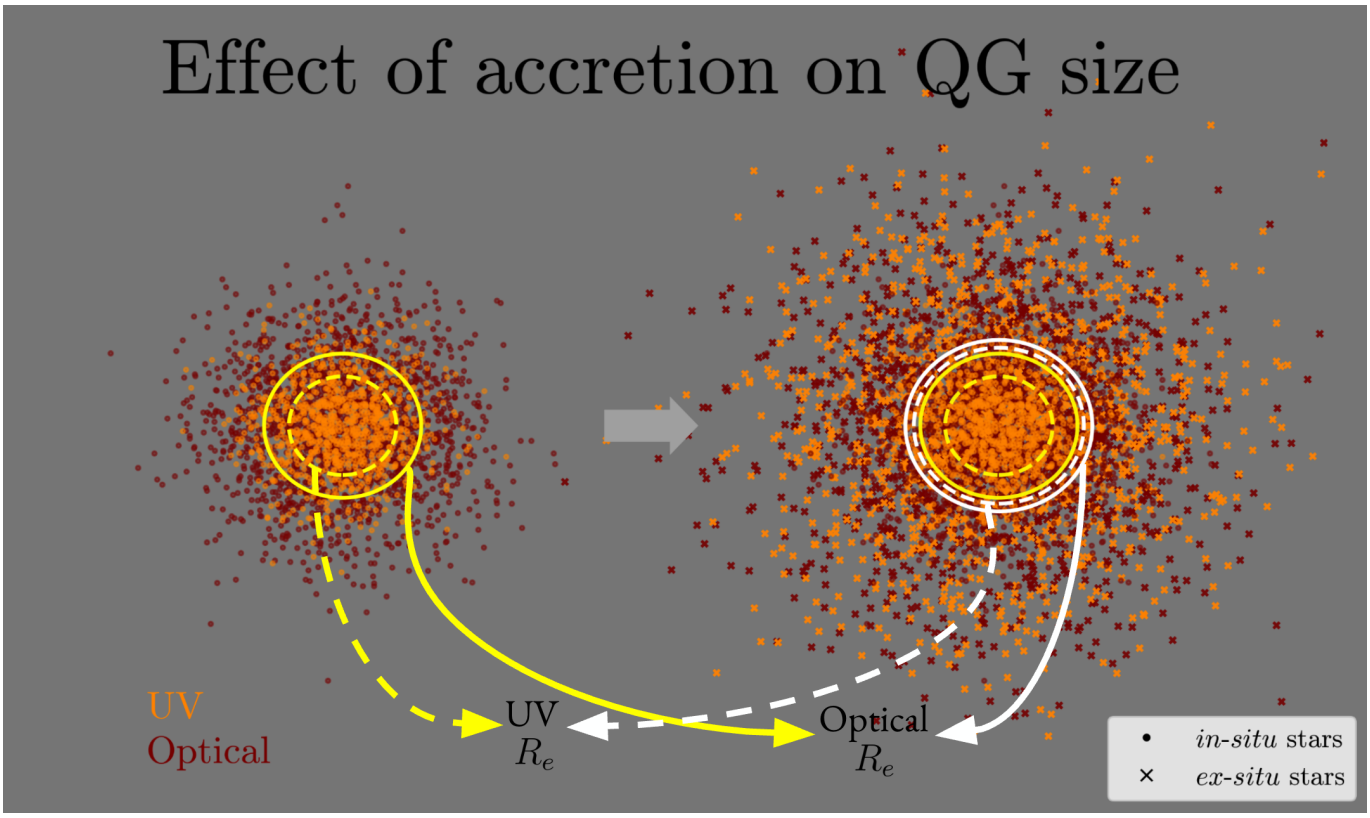

Figure 9. A schematic diagram showing the effect of minor mergers/accretion on the size of bulge components of a QG in the rest-frame UV (orange) and optical (maroon) wavelengths. The effective radii before and after adding materials to the galaxy are shown in yellow and white, respectively. The materials added through minor mergers/accretion occupy the outer halo of a galaxy thereby increasing the measured effective radius of its bulge component. Unlike the *in-situ* stellar population (dots) of a QG, the newly added *ex-situ* population (crosses) have a significant fraction of UV bright stars (young massive stars or low metallicity stars). Thus, the merger/accretion-driven growth is faster in rest-UV than in the rest-optical.

general show negative metallicity gradients. Studies indicate that some of the galaxy bulges are relics of blue/red nugget galaxies from high redshifts ($z > 1$; I. Damjanov et al. 2009, 2011; A. Ferré-Mateu et al. 2017; L. Costantin et al. 2021, 2022; C. Spiniello et al. 2021). During the post-blue nugget phase, these galaxies tend to have a flat metallicity gradient in the innermost 1 kpc region due to fast depletion of gas (S. Lapiner et al. 2023), and they form a major part of the bulges of more evolved galaxies. The presence of similar low-mass stars in the bulge of the Milky Way has been well explored (L. M. Howes et al. 2015; M. Schultheis et al. 2015; M. Ness & K. Freeman 2016; F. Fragkoudi et al. 2017; H. Reggiani et al. 2020). Because the UV-optical color of low metallicity stars is bluer than that of high metallicity stars, their presence should make galaxy bulges more compact in the rest-UV than in the rest-optical.

Additionally, the Sérsic indices of QG bulges are lower in the UV than in the optical (lower panel of Figure 8). This indicates that while the UV-emitting stars occupy a compact region, their spatial distribution is less centrally concentrated than that of the bulk stellar population. This result is consistent with the recent findings of M. Pizzardo et al. (2026), who utilized single Sérsic profile fits to show that quiescent galaxies exhibit lower n values in the rest-UV compared to the optical.

This less centrally peaked distribution in UV could arise for multiple reasons. The UV profile could reflect the low n distribution of the star-forming regions prior to quenching. They could also be driven by the distribution of globular clusters with UV bright or low metallicity stars (e.g., S. Kaviraj et al. 2007; D. A. Forbes et al. 2022).

Moreover, shallow UV profiles could also be the result of the distribution of young/low-metallicity stars in the outskirts added through minor mergers and accretion (halo growth; D. J. Williams et al. 2025). While minor mergers are understood to increase the global Sérsic index in terms of stellar mass by building extended wings in the mass distribution (e.g., P. F. Hopkins et al. 2010a; H. J. Zahid et al. 2019), they may have the opposite effect on the UV light profile. If the accreted material is more UV-luminous than the central population — due to downsizing in time (E. Neistein et al. 2006) or low

metallicity — its presence in the halo would 'flatten' the light distribution. Because our bulge model captures all non-disk light (Section 7.1), including this accreted halo, the combination of a central bulge and a UV-bright outer halo would yield a lower n in the UV than in the optical, where the older, centrally-concentrated mass dominates.

Furthermore, the sizes of QG bulges grow rapidly with cosmic time. This growth rate is higher in UV light than in visible light; although QG bulges are slightly smaller in UV than in the optical at the high redshift limit of our sample, the UV sizes become slightly larger than optical sizes at $z < 0.4$ (the right panel of Figure 6). The wavelength dependence of the size increase for bulges supports the minor merger-/accretion-driven growth of QGs because the accreted material has a higher fraction of UV bright stars (young or low-metallicity). Since the QGs are in general UV faint, the addition of accreted material to the galaxy halos increases the effective radii of bulges in the UV more than in the optical.

We illustrate the impact of *ex-situ* accreted material in QGs on the effective radius measured at the rest-UV (orange) and rest-optical (maroon) wavelengths using a simplified toy model in Figure 9. The image on the left is a representative diagram of QG bulges in these two wavelengths. There are more maroon points than orange ones, indicating that the bulge is brighter in the longer wavelengths[15]. The solid and dashed curves represent the measured effective radii in the UV and optical wavelengths, respectively, with the bulge appearing more compact in the UV than in the optical.

When this galaxy undergoes a series of minor mergers or accretion events, material is added to the outer regions. The accreted population in this toy model consists of an equal proportion of both orange and maroon data points, as illustrated in the galaxy model on the right. This is because the accreted material comes from low-mass systems could contain higher fractions of younger/low-metallicity stars than massive quiescent systems (I. Saviane et al. 2008; A. P. Cooper et al. 2010; M. Hirschmann et al. 2015). The addition of stellar material changes the effective radius of orange points (dashed circles) more than that of the maroon points (solid circles), *i.e.*, the measured size grows more in UV light than in the optical light. Therefore, the growth of bulge/spheroidal components driven by minor mergers and accretion is faster in the shorter wavelength than in the longer wavelength.

[15] Note that a significant fraction of maroon points is behind the distribution of orange points

In addition, part of the observed growth in the QG bulge sizes may result from progenitor bias introduced by the newcomers. At any given redshift, SFG bulges tend to be larger than QG bulges, so the ongoing addition of these newly quenched galaxies to the QG population should increase the average quiescent bulge size. To summarize, as in the case of the total sizes of QGs, the size evolution of their structural components is also driven by mergers/accretion along with the progenitor bias from the newcomers.

8. LIMITATIONS

We note that the limitations we discuss in our Paper I are also valid for this work. Classification of galaxies into star-forming and quiescent depends on the methodologies used (color-color diagrams, specific star-formation rates, etc.) and could differ from other works in the literature. Using our data set, we cannot distinguish between contributions from young and low-metallicity stars in the UV light profiles (due to the age-metallicity degeneracy; B. Gustafsson 1989; D. Streich et al. 2014). The presence of dust can also affect measured sizes, particularly in the rest-UV band, where the dust obscuration is higher than that of the visible band. Our dataset cannot trace the radial distribution of dust in our targets; spatially resolved data at longer wavelengths (far-infrared to radio) is required for dust mapping.

In addition, there are limitations to the fitting methodology adopted in this work. While we use an exponential profile for the disk and a free Sérsic profile for the bulge, many massive galaxies may require a third "halo" component to fully capture their outer stellar envelopes. Although our deep ground-based data theoretically reaches the surface brightness levels required to detect such halos, robustly decomposing three separate components at these redshifts remains challenging. The primary obstacle is model degeneracy; the spatial resolution of ground-based imaging often cannot distinguish between a concentrated bulge and an extended halo component, particularly when they overlap in the central regions.

To manage these degeneracies, some studies fix the bulge to a de Vaucouleurs profile ($n = 4$). While this reduces the uncertainty in size and flux measurements, it imposes a structural bias by forcing all bulges into a centrally concentrated shape regardless of their intrinsic profile. If a galaxy possesses a lower-Sérsic index bulge, fixing $n = 4$ results in significant systematic residuals and can lead to inaccurate measurements of the bulge effective radius and B/T values. By allowing n to remain free, we prioritize capturing the intrinsic variety

of bulge shapes, even if it introduces higher statistical uncertainty.

Moreover, our selection of disks and bulges, based on B/T cuts (Section 4), excludes components that contribute less than 20% to the galaxy's total surface brightness profile. By implementing this threshold, we ensure that our analysis is restricted to galaxies with two distinct and well-defined structural components. This prevents the inclusion of marginal 'bulges' or 'disks' — which may simply represent noise or minor residuals in a single-component system — thereby allowing for a more robust comparison of the physical evolution of these two distinct populations.

Furthermore, light contamination from nearby faint background objects can affect component size measurements, particularly for intrinsically faint bulges/disks (Section 3). Our simulations show that such contamination tends to increase measured sizes. While we mitigate this by excluding very faint components through B/T cuts (Section 5) and introduce a correction to the measured sizes using simulations (Appendix A), the effect is not entirely removed. For instance, the large optical sizes of QG disks ($\log R_e \sim 1.2$ at $\log M \sim 11$) in the bottom panel of Figure 4 are partly due to this effect. However, we do not expect this to bias our scientific conclusions, as we account for such uncertainties through the error estimates described in Appendix A.

Finally, the SMRs of bulges and disks strongly depend on the choice of the stellar mass (J. Méndez-Abreu et al. 2021). Several works in the literature adopt the stellar mass of the components to study their scaling relation (e.g., P. Dimauro et al. 2019; A. S. G. Robotham et al. 2022b; K. V. Nedkova et al. 2024). However, estimating the stellar masses of individual components is far more challenging than measuring the total stellar mass. SED-based mass estimates depend sensitively on assumptions about the stellar population models, IMF, and dust attenuation laws (C. Pacifici et al. 2023; K. V. Nedkova et al. 2024), and separating the bulge and disk stellar populations is not straightforward. In addition, the IRAC data used to constrain the mass estimates have a relatively poor PSF, which further limits our ability to obtain reliable component masses. Therefore, we adopt the total stellar mass while analyzing the SMR for bulges and disks. As we discuss in Section 5, in this work, we probe the evolution of SMR-derived characteristic sizes of bulges and disks in galaxies with similar stellar mass.

9. CONCLUSIONS

Utilizing deep imaging from the CFHT CLAUDS and Subaru HSC-SSP surveys, we have characterized the structural evolution of a mass-complete sample comprising 44,086 SFGs and 34,108 QGs across the redshift range $0.1 < z < 0.85$. By performing bulge+disk decompositions with SourceXtractor++ in both the rest-frame UV (3000Å) and optical (5000Å), we examine the size–mass relation (SMR) for the bulge and disk components separately. From these relations, we determine the characteristic size of each component for galaxies at a fiducial total stellar mass of $5\times10^{10}M_{\odot}$, allowing us to track how the physical scales of these structures evolve with cosmic time. This comparison probes different aspects of bulge and disk growth for the two galaxy populations (Figure 6):

1. *Relative component scales* - The characteristic sizes of disks are consistently larger than those of bulges for both SFGs and QGs across both wavelengths.

2. *Wavelength-dependent sizes* - For a given galaxy population, disk sizes are more extended in the UV than in the optical, whereas bulge sizes remain comparable between the two wavelengths.

3. *Differential growth rates* - The pace of size evolution varies significantly between populations and wavelengths. Bulges exhibit faster size evolution in the rest-UV than in the rest-optical. In contrast, QG disks grow significantly faster in the longer wavelength than in the shorter wavelength, whereas this wavelength-dependent difference is much less pronounced for SFG disks.

Thus, our results show that if a galaxy has both a bulge and a disk, its disk would be larger than its bulge and would appear more extended in UV than in the optical (Figure 7). In contrast, the bulges are slightly smaller in UV light at higher z, but due to their fast growth, the UV size catches up with the optical size by $z = 0.4$.

These results confirm our previous finding based on single-Sérsic fitting (Paper I) that bulge growth is a major driving mechanism in SFGs. The bulges are growing at a rapid rate, and their growth can affect the measured sizes of the SFGs using a single Sérsic profile. The emergence/growth of bulges could significantly slow the size growth rate of SFGs, although the individual structural components (bulge and disk) grow faster than their combined size.

We also interpret the rapid size growth of QG bulges (more in the UV band than in the optical band) as driven by minor mergers and accretion. This merger-driven growth affects more in the shorter wavelength than in the longer wavelength (Figure 9).

However, we cannot currently disentangle the effects of the age-metallicity degeneracy and impact of dust with our dataset. We need spatially resolved spectroscopy and dust maps to address these issues. Ongoing and upcoming large-scale surveys using cutting-edge integral field spectrographs/units like Very Large Telescope's MUSE (T. Urrutia et al. 2019; C. Foster et al. 2021; E. Emsellem et al. 2022) and adaptive optics (AO) assisted ERIS (R. Davies et al. 2018; J. Hayoz et al. 2025), James Webb Space Telescope's NIRSpec IFU (T. Böker et al. 2022; P. Jakobsen et al. 2022) and Gemini Observatory's AO assisted GIRMOS (U. Conod et al. 2023) can address the issue of age-metallicity degeneracy in galaxy profiles through spatially resolved spectral fitting. Along with MUSE, cutting-edge technologies of Atacama Large Millimeter/submillimeter Array, James Webb Space Telescope's MIRI, etc. can help us map the dust distribution in galaxies (e.g., L. Lin et al. 2020; B. Magnelli et al. 2023; K.-i. Tadaki et al. 2023; J. Li et al. 2024; C. Lind-Thomsen et al. 2025).

Collectively, these multi-wavelength and spatially resolved perspectives will allow us to move beyond photometric decomposition and directly test the evolutionary pathways proposed in this work. For the quiescent population in particular, these data will be instrumental in distinguishing between 'newcomer' galaxies — whose structures are still influenced by their recent star-formation history — and aging QGs shaped by interactions that follow quenching. By tracing age and metallicity gradients into the stellar halos and reconstructing galaxy kinematic properties to large radii, we can quantify the role of ex-situ growth in driving the wavelength-dependent structural evolution of both galaxy bulges and disks.

ACKNOWLEDGMENTS

This research was supported by Discovery Grants to I.D. and M.S. from the Natural Sciences and Engineering Research Council (NSERC) of Canada. We utilize computational resources from ACENET, the Digital Research Alliance of Canada and CANFAR. We thank members of the extragalactic research group at Saint Mary's University, Canada, in particular, Gaia Gaspar and Rosi Mérida, for their valuable insights and suggestions. We also acknowledge valuable inputs from the Euclid collaboration regarding the usage of SE++.

This work is based on data obtained and processed as part of the CFHT Large Area U-band Deep Survey (CLAUDS), which is a collaboration between astronomers from Canada, France, and China described in M. Sawicki et al. (2019). CLAUDS data products can be accessed from https://www.clauds.net. CLAUDS is based on observations obtained with MegaPrime/ MegaCam, a joint project of CFHT and CEA/DAPNIA, at the CFHT which is operated by the National Research Council (NRC) of Canada, the Institut National des Science de l'Univers of the Centre National de la Recherche Scientifique (CNRS) of France, and the University of Hawaii. CLAUDS uses data obtained in part through the Telescope Access Program (TAP), which has been funded by the National Astronomical Observatories, the Chinese Academy of Sciences, and the Special Fund for Astronomy from the Ministry of Finance of China. CLAUDS uses data products from TERAPIX and the Canadian Astronomy Data Centre (CADC) and was carried out using resources from Compute Canada and the Canadian Advanced Network For Astrophysical Research (CANFAR).

This paper is also based on data collected at the Subaru Telescope and retrieved from the HSC data archive system, which is operated by the Subaru Telescope and Astronomy Data Center (ADC) at the National Astronomical Observatory of Japan. Data analysis was in part carried out with the cooperation of the Center for Computational Astrophysics (CfCA), National Astronomical Observatory of Japan. The Hyper Suprime-Cam (HSC) collaboration includes the astronomical communities of Japan and Taiwan, and Princeton University, USA. The Hyper Suprime-Cam (HSC) collaboration includes the astronomical communities of Japan and Taiwan, and Princeton University. The HSC instrumentation and software were developed by the National Astronomical Observatory of Japan (NAOJ), the Kavli Institute for the Physics and Mathematics of the Universe (Kavli IPMU), the University of Tokyo, the High Energy Accelerator Research Organization (KEK), the Academia Sinica Institute for Astronomy and Astrophysics in Taiwan (ASIAA), and Princeton University.

AUTHOR CONTRIBUTIONS

This work is a part of the Ph.D. research of AG at Saint Mary's University, Halifax. AG was responsible for writing and submitting the manuscript. His Ph.D. supervisors, ID and MS were actively involved in the data analysis and interpretation. They also obtained the funding and edited the manuscript. GD produced the photometric catalog used in this work, while LC measured the stellar masses of galaxies. The other authors contributed to the dataset used in this work.

Facilities: Subaru Telescope (HSC), CFHT (MegaCam)

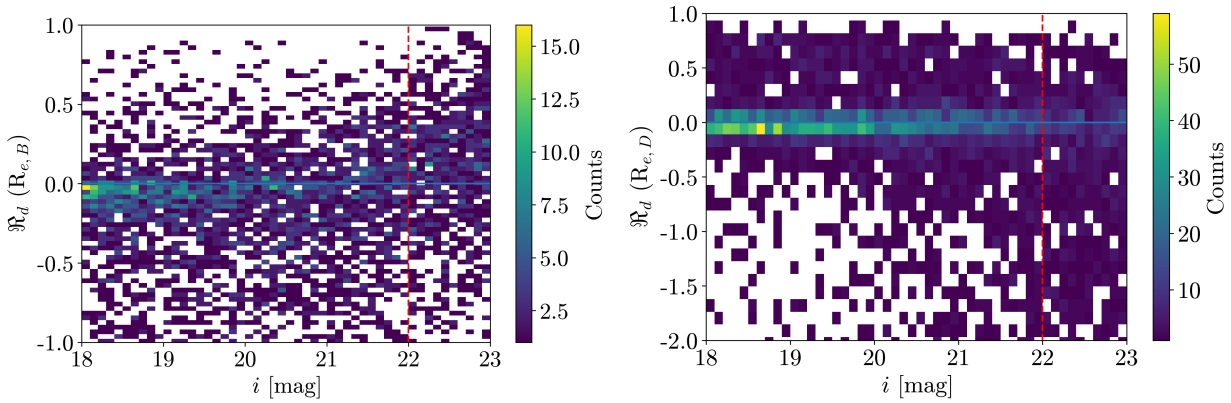

Figure 10. Distribution of relative difference ($\Re_d$; Eq. A1) in size measurements of bulges (left) and disks (right) as a function of i-band magnitudes.

Software: NumPy (S. van der Walt et al. 2011; C. R. Harris et al. 2020), SciPy (P. Virtanen et al. 2020), Astropy (Astropy Collaboration et al. 2013, 2018, 2022), Photutils (L. Bradley et al. 2022), Scikit-learn (F. Pedregosa et al. 2011), Matplotlib (J. D. Hunter 2007), GalfitPyWrap[16], SExtractor (E. Bertin & S. Arnouts 1996), SourceExtractor++ (E. Bertin et al. 2020), PSFEx (E. Bertin 2011), Dynesty (J. S. Speagle 2020), Linmix[17], GALFIT (C. Y. Peng et al. 2002, 2010)

APPENDIX

A. SIMULATIONS

To assess the robustness of our SE++ measurements and quantify uncertainties, we conduct simulations by modeling and planting mock galaxies into the real CLAUDS+HSC images. Using GALFIT (C. Y. Peng et al. 2002, 2010), we generate images of artificial galaxies with a Sérsic bulge and an exponential disk. In doing so, we explore the Sérsic parameter space of local galaxies modeled in the literature (L. Simard et al. 2011). We generate 5,000 synthetic galaxies with properties uniformly spanning the observed parameter space: bulge effective radii $0.1 \leq r_{e,B}/\mathrm{arcsec} \leq 2.0$, disk effective radii $0.5 \leq r_{e,D}/\mathrm{arcsec} \leq 10.0$, Sérsic indices $0.5 \leq n_B \leq 8.0$, and B/T ratios $0.1 \leq B/T \leq 0.9$.

To avoid artificial overcrowding, we only plant 50 simulated galaxies at a time in a CLAUDS+HSC image ($\sim 0.168 \times 0.168$ arcmin^2). This approach tests the recovery of the bulge and disk parameters under realistic conditions, taking into account the effects of noise, crowding, and PSF.

To analyze the simulation results, we explore the relative difference between input and output values of a given parameter x, defined as

$$\Re_d(x) = \frac{x\,(\mathrm{input}) - x\,(\mathrm{output})}{x\,(\mathrm{output})}. \tag{A1}$$

In Figure 10, we show the distribution of relative differences in effective radii of bulges (left) and disks (right) as a function of galaxy magnitudes in i-band. Although SE++ is able to recover the sizes, the scatter in the relative difference increases at $i > 22$ mag. Our simulations also show that we can reasonably model other Sérsic parameters for bulge and disk components for galaxies with brightness $i < 22$ mag. Beyond this brightness limit, the noise dominates and the uncertainties in the measured parameters are too large. Hence, we limit our analysis only to bright ($i < 22$ mag) galaxies in this work.

A.1. *Uncertainty Estimation*

To estimate the uncertainties in our fitting results, we follow a method similar to the one prescribed in A. George et al. (2024) and compare the input parameters of the simulated galaxies with the fitting results from SE++. To

[16] https://github.com/Grillard/GalfitPyWrap

[17] https://linmix.readthedocs.io/en/latest/src/linmix.html

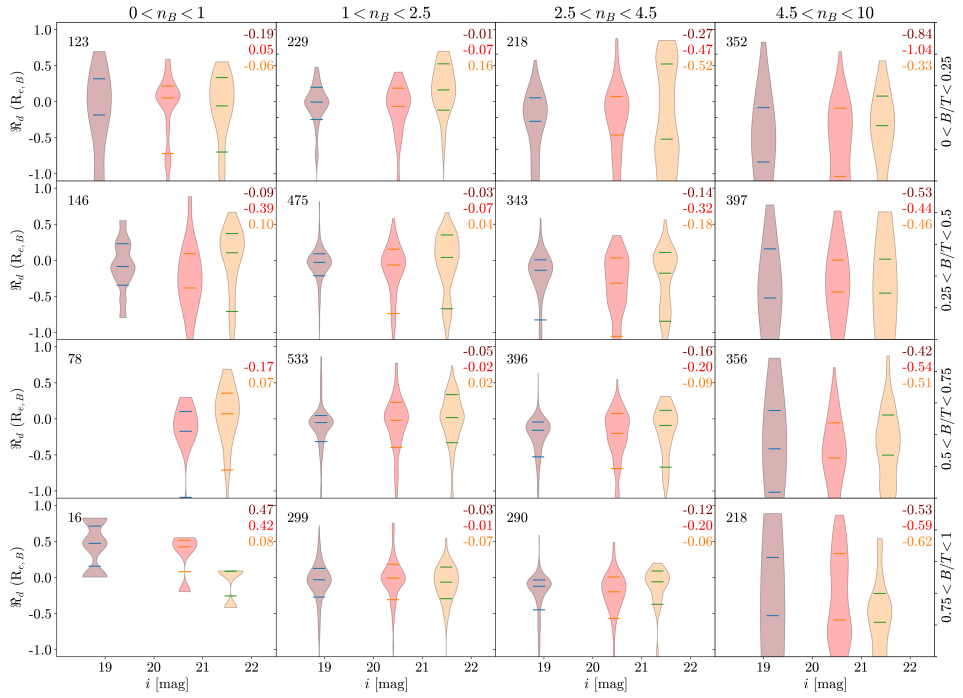

Figure 11. Distribution of relative difference in size measurements of bulges ($\Re_d(R_{e,B})$; Eq. A1) in bins of i-band magnitudes, bulge Sérsic index (n_B) and bulge-to-total ratio (B/T). In each subpanel, the median $\Re_d(R_{e,B})$ of the violin plots is provided in the top-right corner in its respective color. We also provide the total number of simulated galaxies in each subpanel at the top left corner.

quantify the comparison, we use the relative difference in Eq. A1 and investigate how this $\Re_d(x)$ varies with input magnitudes and output structural parameters, B/T and n_B for bulge components (Figure 11) or B/T and $R_{e,D}$ for disk components (Figure 12). We then adopt the scatter in $\Re_d(x)$ in the three-dimensional bins of magnitude, B/T and $R_{e,D}$ or n_B as the uncertainty in the measurement of the fit parameter x.

A.2. *Bias Corrections to the Size Measurements*

Because our ground based measurements are affected by atmospheric seeing, the simulations also show that there can be some systematic biases in the size measurements. For example, we tend to overestimate the sizes of bulges if the modeled $n > 4.5$ (right panels in Figure 11). To reduce the impact of these biases in our results, we correct for the offsets present in our simulations such that the median values of $\Re_d(R_{e,B})$ and $\Re_d(R_{e,D})$ in the 3-D bins of Figures 11 and 12, respectively, are 0. We estimate these bias-corrected effective sizes as

$$R_{e,x}^{\rm corr} = R_{e,x}\left(1 + \text{med}\left[\Re_d(R_{e,x})\right]_{\text{3D bin}}\right), \tag{A2}$$

where x is either B (bulge) or D (disk), and $\text{med}\left[\Re_d(R_{e,x})\right]_{\text{3D bin}}$ is the median offset in the 3-D bins as shown in the simulation violin plots (Figures 11 and 12).

Consequently, the size measurements presented in Section 4 and utilized throughout this analysis represent these bias-corrected values. However, we note that the major qualitative results of this work remain valid even if we use uncorrected size measurements.

REFERENCES

Aihara, H., Arimoto, N., Armstrong, R., et al. 2018, PASJ, 70, S4, doi: 10.1093/pasj/psx066

Aihara, H., AlSayyad, Y., Ando, M., et al. 2019, PASJ, 71, 114, doi: 10.1093/pasj/psz103

Aihara, H., AlSayyad, Y., Ando, M., et al. 2022, PASJ, 74, 247, doi: 10.1093/pasj/psab122

Allen, P. D., Driver, S. P., Graham, A. W., et al. 2006, MNRAS, 371, 2, doi: 10.1111/j.1365-2966.2006.10586.x

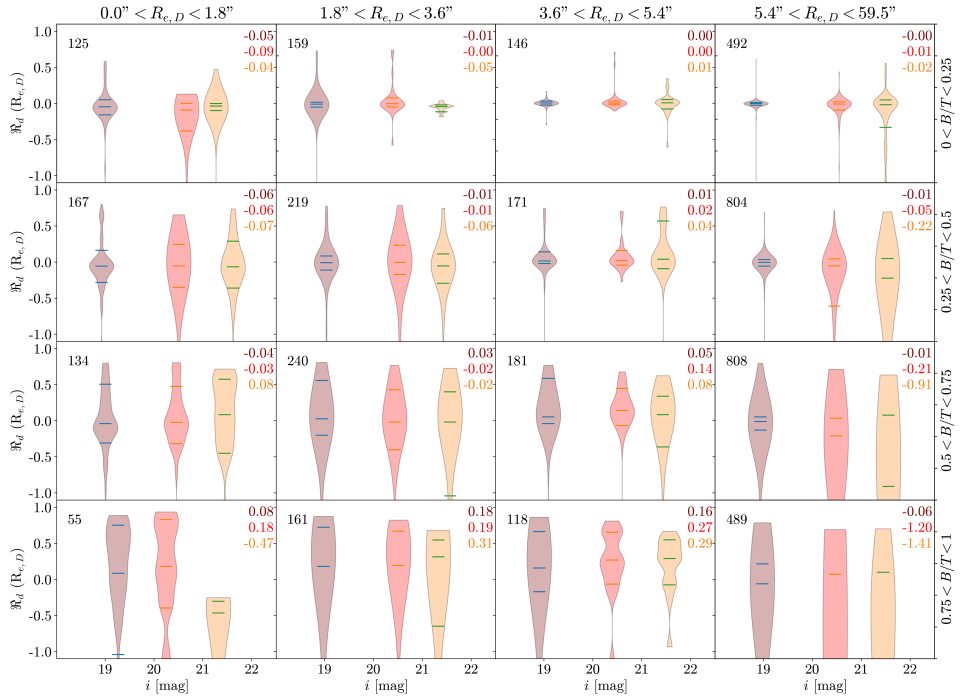

Figure 12. Distribution of relative difference in size measurements of disks ($\Re_d(R_{e,D})$; Eq. A1) in bins of i-band magnitudes, $R_{e,D}$ and B/T. As in Figure 12, the median $\Re_d(R_{e,D})$ values and the total number of simulated galaxies are provided in the top-right and top-left corners of each subpanel, respectively.

Annunziatella, M., Sajina, A., Stefanon, M., et al. 2023, AJ, 166, 25, doi: 10.3847/1538-3881/acd773

Arnouts, S., Le Floc'h, E., Chevallard, J., et al. 2013, A&A, 558, A67, doi: 10.1051/0004-6361/201321768

Astropy Collaboration, Robitaille, T. P., Tollerud, E. J., et al. 2013, A&A, 558, A33, doi: 10.1051/0004-6361/201322068

Astropy Collaboration, Price-Whelan, A. M., Sipőcz, B. M., et al. 2018, AJ, 156, 123, doi: 10.3847/1538-3881/aabc4f

Astropy Collaboration, Price-Whelan, A. M., Lim, P. L., et al. 2022, ApJ, 935, 167, doi: 10.3847/1538-4357/ac7c74

Athanassoula, E. 2005, MNRAS, 358, 1477, doi: 10.1111/j.1365-2966.2005.08872.x

Baldry, I. K., Balogh, M. L., Bower, R. G., et al. 2006, MNRAS, 373, 469, doi: 10.1111/j.1365-2966.2006.11081.x

Barnes, J. E., & Hernquist, L. 1992, ARA&A, 30, 705, doi: 10.1146/annurev.aa.30.090192.003421

Barnes, J. E., & Hernquist, L. 1996, ApJ, 471, 115, doi: 10.1086/177957

Bell, E. F., McIntosh, D. H., Katz, N., & Weinberg, M. D. 2003, ApJS, 149, 289, doi: 10.1086/378847

Bertin, E. 2011, in Astronomical Data Analysis Software and Systems XX, Vol. 442, 435

Bertin, E. 2013, Astrophysics Source Code Library, ascl:1301.001

Bertin, E., & Arnouts, S. 1996, A&AS, 117, 393, doi: 10.1051/aas:1996164

Bertin, E., Schefer, M., Apostolakos, N., et al. 2020, in Astronomical Data Analysis Software and Systems XXIX, Vol. 527, 461

Böker, T., Arribas, S., Lützgendorf, N., et al. 2022, A&A, 661, A82, doi: 10.1051/0004-6361/202142589

Bosch, J., Armstrong, R., Bickerton, S., et al. 2018, PASJ, 70, S5, doi: 10.1093/pasj/psx080

Bottrell, C., Simard, L., Mendel, J. T., & Ellison, S. L. 2019, MNRAS, 486, 390, doi: 10.1093/mnras/stz855

Bournaud, F., Elmegreen, B. G., & Elmegreen, D. M. 2007, ApJ, 670, 237, doi: 10.1086/522077

Bradley, L., Sipőcz, B., Robitaille, T., et al. 2022,

Brooks, A., & Christensen, C. 2016, in Galactic Bulges, ed. E. Laurikainen, R. Peletier, & D. Gadotti (Cham: Springer International Publishing), 317–353, doi: 10.1007/978-3-319-19378-6_12

Bruce, V. A., Dunlop, J. S., McLure, R. J., et al. 2014, MNRAS, 444, 1660, doi: 10.1093/mnras/stu1537

Bruzual, G., & Charlot, S. 2003, MNRAS, 344, 1000, doi: 10.1046/j.1365-8711.2003.06897.x

Buta, R. J. 2013, in Planets, Stars and Stellar Systems. Volume 6: Extragalactic Astronomy and Cosmology, Vol. 6, 1, doi: 10.1007/978-94-007-5609-0_1

Calzetti, D., Armus, L., Bohlin, R. C., et al. 2000, ApJ, 533, 682, doi: 10.1086/308692

Carollo, C. M., Stiavelli, M., de Zeeuw, P. T., & Mack, J. 1997, AJ, 114, 2366, doi: 10.1086/118654

Carollo, C. M., Cibinel, A., Lilly, S. J., et al. 2016, ApJ, 818, 180, doi: 10.3847/0004-637X/818/2/180

Casey, A. R., & Schlaufman, K. C. 2015, ApJ, 809, 110, doi: 10.1088/0004-637X/809/2/110

Casura, S., Liske, J., Robotham, A. S. G., et al. 2022, MNRAS, 516, 942, doi: 10.1093/mnras/stac2267

Chabrier, G. 2003, PASP, 115, 763, doi: 10.1086/376392

Christlein, D., & Zabludoff, A. I. 2004, ApJ, 616, 192, doi: 10.1086/424909

Clauwens, B., Schaye, J., Franx, M., & Bower, R. G. 2018, MNRAS, 478, 3994, doi: 10.1093/mnras/sty1229

Conod, U., Jackson, K., Turri, P., et al. 2023, PASP, 135, 105001, doi: 10.1088/1538-3873/acf61c

Conselice, C. J. 2014, ARA&A, 52, 291, doi: 10.1146/annurev-astro-081913-040037

Conselice, C. J., Bershady, M. A., Dickinson, M., & Papovich, C. 2003, AJ, 126, 1183, doi: 10.1086/377318

Conselice, C. J., Mundy, C. J., Ferreira, L., & Duncan, K. 2022, ApJ, 940, 168, doi: 10.3847/1538-4357/ac9b1a

Cook, R. H. W., Davies, L. J. M., Bellstedt, S., et al. 2025, MNRAS, 539, 2829, doi: 10.1093/mnras/staf575

Cooper, A. P., Cole, S., Frenk, C. S., et al. 2010, MNRAS, 406, 744, doi: 10.1111/j.1365-2966.2010.16740.x

Costantin, L., Pérez-González, P. G., Méndez-Abreu, J., et al. 2021, ApJ, 913, 125, doi: 10.3847/1538-4357/abef72

Costantin, L., Pérez-González, P. G., Méndez-Abreu, J., et al. 2022, ApJ, 929, 121, doi: 10.3847/1538-4357/ac5a57

Cox, T. J., Younger, J., Hernquist, L., & Hopkins, P. F. 2008, in Formation and Evolution of Galaxy Bulges, Vol. 245, 63–66, doi: 10.1017/S1743921308017298

Cui, Q., Zhao, P., & Liu, F. S. 2024, ApJ, 973, 52, doi: 10.3847/1538-4357/ad6321

Cutler, S. E., Whitaker, K. E., Mowla, L. A., et al. 2022, ApJ, 925, 34, doi: 10.3847/1538-4357/ac341c

Damjanov, I., Sohn, J., Geller, M. J., Utsumi, Y., & Dell'Antonio, I. 2023, ApJ, 943, 149, doi: 10.3847/1538-4357/aca88f

Damjanov, I., Zahid, H. J., Geller, M. J., et al. 2019, ApJ, 872, 91, doi: 10.3847/1538-4357/aaf97d

Damjanov, I., McCarthy, P. J., Abraham, R. G., et al. 2009, ApJ, 695, 101, doi: 10.1088/0004-637X/695/1/101

Damjanov, I., Abraham, R. G., Glazebrook, K., et al. 2011, ApJ, 739, L44, doi: 10.1088/2041-8205/739/2/L44

Davari, R., Ho, L. C., Peng, C. Y., & Huang, S. 2014, AJ, 787, 69, doi: 10.1088/0004-637X/787/1/69

Davies, R., Esposito, S., Schmid, H.-M., et al. 2018, in Proc. SPIE, Vol. 10702, eprint: arXiv:1807.05089, 1070209, doi: 10.1117/12.2311480

De Lucia, G., Fontanot, F., Wilman, D., & Monaco, P. 2011, MNRAS, 414, 1439, doi: 10.1111/j.1365-2966.2011.18475.x

Desprez, G., Picouet, V., Moutard, T., et al. 2023, A&A, 670, A82, doi: 10.1051/0004-6361/202243363

D'Eugenio, C., Daddi, E., Gobat, R., et al. 2020, ApJ, 892, L2, doi: 10.3847/2041-8213/ab7a96

Dewsnap, C., Barmby, P., Gallagher, S. C., et al. 2023, AJ, 944, 137, doi: 10.3847/1538-4357/ac9400

Dimauro, P., Huertas-Company, M., Daddi, E., et al. 2018, MNRAS, 478, 5410, doi: 10.1093/mnras/sty1379

Dimauro, P., Huertas-Company, M., Daddi, E., et al. 2019, MNRAS, 489, 4135, doi: 10.1093/mnras/stz2421

Dimauro, P., Daddi, E., Shankar, F., et al. 2022, MNRAS, 513, 256, doi: 10.1093/mnras/stac884

Duan, Q., Conselice, C. J., Li, Q., et al. 2025, MNRAS, 540, 774, doi: 10.1093/mnras/staf638

Eggen, O. J., Lynden-Bell, D., & Sandage, A. R. 1962, ApJ, 136, 748, doi: 10.1086/147433

Emsellem, E., Schinnerer, E., Santoro, F., et al. 2022, A&A, 659, A191, doi: 10.1051/0004-6361/202141727

Estrada-Carpenter, V., Papovich, C., Momcheva, I., et al. 2023, ApJ, 951, 115, doi: 10.3847/1538-4357/acd4be

Euclid Collaboration, Desprez, G., Paltani, S., et al. 2020, A&A, 644, A31, doi: 10.1051/0004-6361/202039403

Euclid Collaboration, Bretonnière, H., Kuchner, U., et al. 2023, A&A, 671, A102, doi: 10.1051/0004-6361/202245042

Faisst, A. L., Carollo, C. M., Capak, P. L., et al. 2017, ApJ, 839, 71, doi: 10.3847/1538-4357/aa697a

Ferré-Mateu, A., Trujillo, I., Martín-Navarro, I., et al. 2017, MNRAS, 467, 1929, doi: 10.1093/mnras/stx171

Fisher, D. B., & Drory, N. 2011, ApJ, 733, L47, doi: 10.1088/2041-8205/733/2/L47

Forbes, D. A., Ferré-Mateu, A., Gannon, J. S., et al. 2022, MNRAS, 512, 802, doi: 10.1093/mnras/stac503

Förster Schreiber, N. M., & Wuyts, S. 2020, ARA&A, 58, 661, doi: 10.1146/annurev-astro-032620-021910

Foster, C., Mendel, J. T., Lagos, C. D. P., et al. 2021, PASA, 38, e031, doi: 10.1017/pasa.2021.25

Fragkoudi, F., Matteo, P. D., Haywood, M., et al. 2017, A&A, 607, L4, doi: 10.1051/0004-6361/201731597

Freeman, K. C. 1970, ApJ, 160, 811, doi: 10.1086/150474

George, A., Damjanov, I., Sawicki, M., et al. 2024, MNRAS, 528, 4797, doi: 10.1093/mnras/stae154

George, A., Damjanov, I., Sawicki, M., et al. 2025, ApJ, 987, 45, doi: 10.3847/1538-4357/addc6b

Ghosh, A., Urry, C. M., Mishra, A., et al. 2023, ApJ, 953, 134, doi: 10.3847/1538-4357/acd546

Griffith, R. L., Tsai, C.-W., Stern, D., et al. 2011, ApJL, 736, L22, doi: 10.1088/2041-8205/736/1/L22

Guo, Y., McIntosh, D. H., Mo, H. J., et al. 2009, MNRAS, 398, 1129, doi: 10.1111/j.1365-2966.2009.15223.x

Gustafsson, B. 1989, ARA&A, 27, 701, doi: 10.1146/annurev.aa.27.090189.003413

Harris, C. R., Millman, K. J., van der Walt, S. J., et al. 2020, Nat, 585, 357, doi: 10.1038/s41586-020-2649-2

Hashemizadeh, A. 2022, doi: 10.48550/arXiv.2203.11818

Hashemizadeh, A., Driver, S. P., Davies, L. J. M., et al. 2022, MNRAS, 515, 1175, doi: 10.1093/mnras/stac1195

Häußler, B., Vika, M., Bamford, S. P., et al. 2022, A&A, 664, A92, doi: 10.1051/0004-6361/202142935

Hayoz, J., Bonse, M. J., Dannert, F., et al. 2025, A&A, 698, A87, doi: 10.1051/0004-6361/202453297

Hilz, M., Naab, T., & Ostriker, J. P. 2013, MNRAS, 429, 2924, doi: 10.1093/mnras/sts501

Hirschmann, M., Naab, T., Ostriker, J. P., et al. 2015, MNRAS, 449, 528, doi: 10.1093/mnras/stv274

Hon, D. S. H., Graham, A. W., & Sahu, N. 2023, MNRAS, 519, 4651, doi: 10.1093/mnras/stac3704

Hopkins, P. F., Bundy, K., Hernquist, L., Wuyts, S., & Cox, T. J. 2010a, MNRAS, 401, 1099, doi: 10.1111/j.1365-2966.2009.15699.x

Hopkins, P. F., Cox, T. J., Younger, J. D., & Hernquist, L. 2009, ApJ, 691, 1168, doi: 10.1088/0004-637X/691/2/1168

Hopkins, P. F., Bundy, K., Croton, D., et al. 2010b, ApJ, 715, 202, doi: 10.1088/0004-637X/715/1/202

Howes, L. M., Casey, A. R., Asplund, M., et al. 2015, Nature, 527, 484, doi: 10.1038/nature15747

Hu, J., Cui, Q., Wang, L., Pei, W., & Ge, J. 2024, A&A, 691, A125, doi: 10.1051/0004-6361/202451732

Hunter, J. D. 2007, Comput. Sci. Eng., 9, 90, doi: 10.1109/MCSE.2007.55

Ilbert, O., Arnouts, S., McCracken, H. J., et al. 2006, A&A, 457, 841, doi: 10.1051/0004-6361:20065138

Ito, K., Valentino, F., Brammer, G., et al. 2024, ApJ, 964, 192, doi: 10.3847/1538-4357/ad2512

Jakobsen, P., Ferruit, P., Alves de Oliveira, C., et al. 2022, A&A, 661, A80, doi: 10.1051/0004-6361/202142663

Jarvis, M. J., Bonfield, D. G., Bruce, V. A., et al. 2013, MNRAS, 428, 1281, doi: 10.1093/mnras/sts118

Jegatheesan, K., Johnston, E. J., Häußler, B., & Nedkova, K. V. 2024, A&A, 684, A32, doi: 10.1051/0004-6361/202347372

Kaviraj, S., Sohn, S. T., O'Connell, R. W., et al. 2007, MNRAS, 377, 987, doi: 10.1111/j.1365-2966.2007.11712.x

Kaviraj, S., Huertas-Company, M., Cohen, S., et al. 2014, MNRAS, 443, 1861, doi: 10.1093/mnras/stu1220

Kawinwanichakij, L., Silverman, J. D., Ding, X., et al. 2021, ApJ, 921, 38, doi: 10.3847/1538-4357/ac1f21

Kawinwanichakij, L., Glazebrook, K., Nanayakkara, T., et al. 2025, arXiv, doi: 10.48550/arXiv.2505.03089

Kennedy, R., Bamford, S. P., Häußler, B., et al. 2016, MNRAS, 460, 3458, doi: 10.1093/mnras/stw1176

Khochfar, S., & Silk, J. 2006, MNRAS, 370, 902, doi: 10.1111/j.1365-2966.2006.10533.x

Kormendy, J. 1977, ApJ, 217, 406, doi: 10.1086/155589

Kormendy, J., & Fisher, D. B. 2008, 396, 297, doi: 10.48550/arXiv.0810.2534

Kormendy, J., & Kennicutt, Jr., R. C. 2004, ARA&A, 42, 603, doi: 10.1146/annurev.astro.42.053102.134024

Lackner, C. N., & Gunn, J. E. 2012, MNRAS, 421, 2277, doi: 10.1111/j.1365-2966.2012.20450.x

Lang, P., Wuyts, S., Somerville, R. S., et al. 2014, ApJ, 788, 11, doi: 10.1088/0004-637X/788/1/11

Lange, R., Driver, S. P., Robotham, A. S. G., et al. 2015, MNRAS, 447, 2603, doi: 10.1093/mnras/stu2467

Lange, R., Moffett, A. J., Driver, S. P., et al. 2016, MNRAS, 462, 1470, doi: 10.1093/mnras/stw1495

Lapiner, S., Dekel, A., Freundlich, J., et al. 2023, MNRAS, 522, 4515, doi: 10.1093/mnras/stad1263

Li, J., Da Cunha, E., González-López, J., et al. 2024, ApJ, 976, 70, doi: 10.3847/1538-4357/ad7fee

Lima-Dias, C., Monachesi, A., Torres-Flores, S., et al. 2024, MNRAS, 527, 5792, doi: 10.1093/mnras/stad3571

Lin, L., Ellison, S. L., Pan, H.-A., et al. 2020, ApJ, 903, 145, doi: 10.3847/1538-4357/abba3a

Lind-Thomsen, C., Sneppen, A., & Steinhardt, C. L. 2025, ApJ, 985, 144, doi: 10.3847/1538-4357/adc808

López-Sanjuan, C., Balcells, M., Pérez-González, P. G., et al. 2009, A&A, 501, 505, doi: 10.1051/0004-6361/200911923

López-Sanjuan, C., Balcells, M., Pérez-González, P. G., et al. 2010, ApJ, 710, 1170, doi: 10.1088/0004-637X/710/2/1170

Lotz, J. M., Jonsson, P., Cox, T. J., et al. 2011, ApJ, 742, 103, doi: 10.1088/0004-637X/742/2/103

Magnelli, B., Gómez-Guijarro, C., Elbaz, D., et al. 2023, A&A, 678, A83, doi: 10.1051/0004-6361/202347052

Man, A. W. S., Greve, T. R., Toft, S., et al. 2016, ApJ, 820, 11, doi: 10.3847/0004-637X/820/1/11

Martig, M., Bournaud, F., Teyssier, R., & Dekel, A. 2009, ApJ, 707, 250, doi: 10.1088/0004-637X/707/1/250

Martin, D. C., Fanson, J., Schiminovich, D., et al. 2005, ApJ, 619, L1, doi: 10.1086/426387

Martorano, M., van der Wel, A., Baes, M., et al. 2024, ApJ, 972, 134, doi: 10.3847/1538-4357/ad5c6a

Matharu, J., Muzzin, A., Brammer, G. B., et al. 2019, MNRAS, 484, 595, doi: 10.1093/mnras/sty3465

Matharu, J., Muzzin, A., Brammer, G. B., et al. 2020, MNRAS, 493, 6011, doi: 10.1093/mnras/staa610

Matharu, J., Nelson, E. J., Brammer, G., et al. 2024, A&A, 690, A64, doi: 10.1051/0004-6361/202450522

McCracken, H. J., Milvang-Jensen, B., Dunlop, J., et al. 2012, A&A, 544, A156, doi: 10.1051/0004-6361/201219507

Meert, A., Vikram, V., & Bernardi, M. 2015, MNRAS, 446, 3943, doi: 10.1093/mnras/stu2333

Mendel, J. T., Simard, L., Palmer, M., Ellison, S. L., & Patton, D. R. 2014, ApJS, 210, 3, doi: 10.1088/0067-0049/210/1/3

Méndez-Abreu, J., de Lorenzo-Cáceres, A., & Sánchez, S. F. 2021, MNRAS, 504, 3058, doi: 10.1093/mnras/stab1064

Merlin, E., Castellano, M., Bretonnière, H., et al. 2023, A&A, 671, A101, doi: 10.1051/0004-6361/202245041

Moutard, T., Malavasi, N., Sawicki, M., Arnouts, S., & Tripathi, S. 2020, MNRAS, 495, 4237, doi: 10.1093/mnras/staa1434

Moutard, T., Sawicki, M., Arnouts, S., et al. 2018, MNRAS, 479, 2147, doi: 10.1093/mnras/sty1543

Moutard, T., Arnouts, S., Ilbert, O., et al. 2016, A&A, 590, A103, doi: 10.1051/0004-6361/201527294

Mowla, L. A., van Dokkum, P., Brammer, G. B., et al. 2019, ApJ, 880, 57, doi: 10.3847/1538-4357/ab290a

Naab, T., Jesseit, R., & Burkert, A. 2006, MNRAS, 372, 839, doi: 10.1111/j.1365-2966.2006.10902.x

Nedkova, K. V., Häußler, B., Marchesini, D., et al. 2021, MNRAS, 506, 928, doi: 10.1093/mnras/stab1744

Nedkova, K. V., Häußler, B., Marchesini, D., et al. 2024, MNRAS, 532, 3747, doi: 10.1093/mnras/stae1702

Neistein, E., Van Den Bosch, F. C., & Dekel, A. 2006, MNRAS, 372, 933, doi: 10.1111/j.1365-2966.2006.10918.x

Ness, M., & Freeman, K. 2016, PASA, 33, e022, doi: 10.1017/pasa.2015.51

Newman, A. B., Ellis, R. S., Bundy, K., & Treu, T. 2012, ApJ, 746, 162, doi: 10.1088/0004-637X/746/2/162

Ormerod, K., Conselice, C. J., Adams, N. J., et al. 2024, MNRAS, 527, 6110, doi: 10.1093/mnras/stad3597

Oser, L., Ostriker, J. P., Naab, T., Johansson, P. H., & Burkert, A. 2010, ApJ, 725, 2312, doi: 10.1088/0004-637X/725/2/2312

Pacifici, C., Iyer, K. G., Mobasher, B., et al. 2023, ApJ, 944, 141, doi: 10.3847/1538-4357/acacff

Panter, B., Heavens, A. F., & Jimenez, R. 2004, MNRAS, 355, 764, doi: 10.1111/j.1365-2966.2004.08355.x

Pedregosa, F., Varoquaux, G., Gramfort, A., et al. 2011, JMLR, 12, 2825, doi: 10.48550/arXiv.1201.0490

Peng, C. Y., Ho, L. C., Impey, C. D., & Rix, H.-W. 2002, AJ, 124, 266, doi: 10.1086/340952

Peng, C. Y., Ho, L. C., Impey, C. D., & Rix, H.-W. 2010, AJ, 139, 2097, doi: 10.1088/0004-6256/139/6/2097

Peng, Y.-j., Lilly, S. J., Kovač, K., et al. 2010, ApJ, 721, 193, doi: 10.1088/0004-637X/721/1/193

Pizzardo, M., Damjanov, I., Sohn, J., & Geller, M. J. 2026, A&A, 705, A30, doi: 10.1051/0004-6361/202556368

Pozzetti, L., Bolzonella, M., Zucca, E., et al. 2010, A&A, 523, A13, doi: 10.1051/0004-6361/200913020

Prevot, M. L., Lequeux, J., Maurice, E., Prevot, L., & Rocca-Volmerange, B. 1984, A&A, 132, 389

Quilley, L., & de Lapparent, V. 2022, A&A, 666, A170, doi: 10.1051/0004-6361/202244202

Quilley, L., & de Lapparent, V. 2023, A&A, 680, A49, doi: 10.1051/0004-6361/202346774

Quilley, L., de Lapparent, V., Baes, M., et al. 2025, doi: 10.48550/arXiv.2502.15581

Reggiani, H., Schlaufman, K. C., Casey, A. R., & Ji, A. P. 2020, AJ, 160, 173, doi: 10.3847/1538-3881/aba948

Rigamonti, F., Cortese, L., Bollati, F., et al. 2024, A&A, 686, A98, doi: 10.1051/0004-6361/202449191

Robotham, A. S. G., Bellstedt, S., & Driver, S. P. 2022a, MNRAS, 513, 2985, doi: 10.1093/mnras/stac1032

Robotham, A. S. G., Bellstedt, S., & Driver, S. P. 2022b, Astrophysics Source Code Library, ascl:2204.018

Roy, N., Napolitano, N. R., La Barbera, F., et al. 2018, MNRAS, 480, 1057, doi: 10.1093/mnras/sty1917

Sachdeva, S. 2013, MNRAS, 435, 1186, doi: 10.1093/mnras/stt1364

Sachdeva, S., Saha, K., & Singh, H. P. 2017, ApJ, 840, 79, doi: 10.3847/1538-4357/aa6c61

Saintonge, A., Tacconi, L. J., Fabello, S., et al. 2012, ApJ, 758, 73, doi: 10.1088/0004-637X/758/2/73

Saviane, I., Ivanov, V. D., Held, E. V., et al. 2008, A&A, 487, 901, doi: 10.1051/0004-6361:20077617

Sawicki, M., Arnouts, S., Huang, J., et al. 2019, MNRAS, 489, 5202, doi: 10.1093/mnras/stz2522

Schultheis, M., Cunha, K., Zasowski, G., et al. 2015, A&A, 584, A45, doi: 10.1051/0004-6361/201527027

Sellwood, J. A. 2014, Reviews of Modern Physics, 86, 1, doi: 10.1103/RevModPhys.86.1

Shen, S., Mo, H. J., White, S. D. M., et al. 2003, MNRAS, 343, 978, doi: 10.1046/j.1365-8711.2003.06740.x

Simard, L., Mendel, J. T., Patton, D. R., Ellison, S. L., & McConnachie, A. W. 2011, ApJS, 196, 11, doi: 10.1088/0067-0049/196/1/11

Sofue, Y. 2016, PASJ, 68, 2, doi: 10.1093/pasj/psv103

Speagle, J. S. 2020, MNRAS, 493, 3132, doi: 10.1093/mnras/staa278
Spiniello, C., Tortora, C., D'Ago, G., et al. 2021, A&A, 646, A28, doi: 10.1051/0004-6361/202038936
Springel, V., & Hernquist, L. 2005, ApJ, 622, L9, doi: 10.1086/429486
Steinmetz, M., & Navarro, J. F. 2002, New Astron., 7, 155, doi: 10.1016/S1384-1076(02)00102-1
Streich, D., de Jong, R. S., Bailin, J., et al. 2014, A&A, 563, A5, doi: 10.1051/0004-6361/201220956
Suess, K. A., Kriek, M., Price, S. H., & Barro, G. 2019, ApJ, 877, 103, doi: 10.3847/1538-4357/ab1bda
Suess, K. A., Kriek, M., Price, S. H., & Barro, G. 2020, ApJL, 899, L26, doi: 10.3847/2041-8213/abacc9
Suess, K. A., Kriek, M., Price, S. H., & Barro, G. 2021, ApJ, 915, 87, doi: 10.3847/1538-4357/abf1e4
Tacchella, S., Diemer, B., Hernquist, L., et al. 2019, MNRAS, 487, 5416, doi: 10.1093/mnras/stz1657
Tadaki, K.-i., Kodama, T., Koyama, Y., et al. 2023, ApJL, 957, L15, doi: 10.3847/2041-8213/ad03f2
Thibert, N., Sawicki, M., Goulding, A., et al. 2021, RNAAS, 5, 144, doi: 10.3847/2515-5172/ac0911
Tonini, C., Mutch, S. J., Croton, D. J., & Wyithe, J. S. B. 2016, MNRAS, 459, 4109, doi: 10.1093/mnras/stw956
Trujillo, I., Rudnick, G., Rix, H.-W., et al. 2004, ApJ, 604, 521, doi: 10.1086/382060
Urrutia, T., Wisotzki, L., Kerutt, J., et al. 2019, A&A, 624, A141, doi: 10.1051/0004-6361/201834656
van der Walt, S., Colbert, S. C., & Varoquaux, G. 2011, Comput. Sci. Eng., 13, 22, doi: 10.1109/MCSE.2011.37
van der Wel, A., Franx, M., van Dokkum, P. G., et al. 2014, ApJ, 788, 28, doi: 10.1088/0004-637X/788/1/28
Vika, M., Bamford, S. P., Häußler, B., & Rojas, A. L. 2014, MNRAS, 444, 3603, doi: 10.1093/mnras/stu1696
Virtanen, P., Gommers, R., Oliphant, T. E., et al. 2020, Nat. Meth., 17, 261, doi: 10.1038/s41592-019-0686-2
Wagner, C. R., Brodwin, M., Snyder, G. F., et al. 2015, ApJ, 800, 107, doi: 10.1088/0004-637X/800/2/107
Ward, E., de la Vega, A., Mobasher, B., et al. 2024, ApJ, 962, 176, doi: 10.3847/1538-4357/ad20ed
Whitaker, K. E., Bezanson, R., van Dokkum, P. G., et al. 2017, ApJ, 838, 19, doi: 10.3847/1538-4357/aa6258
Williams, D. J., Damjanov, I., Sawicki, M., et al. 2025, ApJ, 989, 107, doi: 10.3847/1538-4357/ade9a8
Williams, R. J., Quadri, R. F., Franx, M., et al. 2010, ApJ, 713, 738, doi: 10.1088/0004-637X/713/2/738
Zahid, H. J., Geller, M. J., Damjanov, I., & Sohn, J. 2019, ApJ, 878, 158, doi: 10.3847/1538-4357/ab21b9
Zhang, L., Zhu, L., Pillepich, A., et al. 2025, A&A, doi: 10.1051/0004-6361/202451292
Zibetti, S., & Gallazzi, A. R. 2022, MNRAS, 512, 1415, doi: 10.1093/mnras/stac370